# **GEOSPHERE**

GEOSPHERE, v. 18, no. 1

https://doi.org/10.1130/GES02426.1

10 figures; 1 set of supplemental files

CORRESPONDENCE: margaret.odlum@unlv.edu

CITATION: Odlum, M.L., Ault, A.K., Channer, M.A., and Calzolari, G., 2021, Seismicity recorded in hematite fault mirrors in the Rio Grande rift: Geosphere, v. 18, no. 1, p. 241–260, https://doi.org/10.1130/GES02426.1.

Science Editor: Andrea Hampel Associate Editor: Jose M. Hurtado

Received 26 February 2021 Revision received 23 June 2021 Accepted 8 August 2021

Published online 16 November 2021





This paper is published under the terms of the CC-BY-NC license.

© 2021 The Authors

# Seismicity recorded in hematite fault mirrors in the Rio Grande rift

M.L. Odlum\*, A.K. Ault, M.A. Channer<sup>†</sup>, and G. Calzolari<sup>§</sup>

Department of Geosciences, Utah State University, 4505 Old Main Hill, Logan, Utah 84322, USA

## ABSTRACT

Exhumed fault rocks provide a textural and chemical record of how fault zone composition and architecture control coseismic temperature rise and earthquake mechanics. We integrated field, microstructural, and hematite (U-Th)/He (He) thermochronometry analyses of exhumed minor (square-centimeter-scale surface area) hematite fault mirrors that crosscut the ca. 1400 Ma Sandia granite in two localities along the eastern flank of the central Rio Grande rift, New Mexico. We used these data to characterize fault slip textures; evaluate relationships among fault zone composition, thickness, and inferred magnitude of friction-generated heat; and document the timing of fault slip. Hematite fault mirrors are collocated with and crosscut specular hematite veins and hematite-cemented cataclasite. Observed fault mirror microstructures reflect fault reactivation and strain localization within the comparatively weaker hematite relative to the granite. The fault mirror volume of some slip surfaces exhibits polygonal, sintered hematite nanoparticles likely created during coseismic temperature rise. Individual fault mirror hematite He dates range from ca. 97 to 5 Ma, and ~80% of dates from fault mirror volume aliquots with high-temperature crystal morphologies are ca. 25-10 Ma. These aliquots have grain-size-dependent closure temperatures of ~75-108 °C. A new mean apatite He date of 13.6 ± 2.6 Ma from the Sandia granite is consistent with prior low-temperature thermochronometry data and reflects rapid, Miocene rift flank exhumation. Comparisons of thermal history models and

hematite He data patterns, together with field and microstructural observations, indicate that seismicity along the fault mirrors at ~2–4 km depth was coeval with rift flank exhumation. The prevalence and distribution of high-temperature hematite grain morphologies on different slip surfaces correspond with thinner deforming zones and higher proportions of quartz and feldspar derived from the granite that impacted the bulk strength of the deforming zone. Thus, these exhumed fault mirrors illustrate how evolving fault material properties reflect but also govern coseismic temperature rise and associated dynamic weakening mechanisms on minor faults at the upper end of the seismogenic zone.

## ■ INTRODUCTION

Exhumed fault rocks provide a thermal, chemical, and rheological record of seismicity (e.g., Rowe and Griffith, 2015). Fault zone composition controls, in part, the strength and stability of fault slip (Shimamoto and Logan, 1981; Rice and Ruina, 1983; Dieterich, 1986; Beeler, 2007; Leeman et al., 2016, 2018; Brantut and Platt, 2017; Ikari, 2019). Deformation experiments and empirical equations illustrate that the thickness and mineralogy of the deforming zone impact the strain distribution, frictional strength, and dynamics of faulting (e.g., Ikari et al., 2011; Leeman et al., 2018). During seismic slip, work done against friction can yield dramatic temperature rise that activates various dynamic weakening mechanisms controlling fault strength (e.g., Rice, 2006; Beeler et al., 2008; Di Toro et al., 2011; Goldsby and Tullis, 2011). Along small

(square-centimeter-scale surface area) but thin slip surfaces, which are common in exhumed fault damage zones, paired microscale to nanoscale textural, geochemical, and thermochronometric analyses can illuminate relationships among fault zone composition, the magnitude of frictional temperature rise, and slip behavior that complements observations from deformation experiments (e.g., McDermott et al., 2017; Ault, 2020). Deformation along these faults may be associated with small, low-moment-magnitude slip events that nucleate at the upper end of the seismogenic zone or are triggered by larger-magnitude earthquakes that nucleate at depth.

Fault mirrors are one type of thin (typically <1 mm thick) slip surface in exhumed fault damage zones. These high-gloss, light-reflective slip surfaces are composed of layered nanoparticles to microparticles that can form at seismic to subseismic slip rates (e.g., Siman-Tov et al., 2013; Verberne et al., 2013; Pozzi et al., 2018). Fault mirrors have been observed in a variety of rock types, including carbonate, siliciclastics, basalt, granite, hematite, and chert, and they occur at a variety of scales (square millimeter to greater than square meter surface area; Power and Tullis, 1989; Fondriest et al., 2013; Evans et al., 2014; Kuo et al., 2016; Borhara and Onasch, 2020; Houser et al., 2021). Some processes invoked for generating fault mirrors include thermal decomposition, melting, gel lubrication, frictional grinding and nanoparticle lubrication, crystal plastic deformation and recrystallization, and/or asperity flash heating (e.g., Collettini et al., 2013; Kirkpatrick et al., 2013; Smith et al., 2013; Pozzi et al., 2018; Ault et al., 2019; Han et al., 2011; De Paola et al., 2011). These processes are dynamic weakening mechanisms that control earthquake mechanics, and some require coseismic heat (e.g., Rattez and Veveakis, 2020).

Textures and particle morphologies of hematite fault mirrors provide information about fault

Margaret L. Odlum https://orcid.org/0000-0002-7873-9900

<sup>\*</sup>Present address: Department of Geoscience, University of Nevada, Las Vegas, Las Vegas, Nevada, USA

<sup>†</sup>Present address: Oak Ridge National Laboratory, 1 Bethel Valley Road, Oak Ridge, Tennessee 37830, USA

<sup>§</sup>Present address: GeoAlps Engineering SA, Via Cantonale 15, CH-6760 Faido, Italy

slip rates and processes, and integrated hematite (U-Th)/He (hematite He) thermochronometry can provide constraints on the timing, temperatures, and depths of fault slip (Evans et al., 2014; Ault et al., 2015, 2019; McDermott et al., 2017; Ault, 2020). In this study, we integrated field and microstructural analyses with hematite He thermochronometry to document evidence for transient temperature rise, deformation mechanisms, and the timing of seismicity on minor hematite fault mirrors in two locations in the Sandia Mountains, New Mexico, in the flank of the Rio Grande rift. Hematite He data were compared with new and previously published conventional low-temperature thermochronometry data and thermal history models to evaluate the timing of slip. Combined textures and thermochronometry data suggest that seismic slip on these small faults was coeval with Miocene Rio Grande rifting. Variations in hematite morphology and fault mirror microstructures are linked to variations in fault mirror composition and thickness. These factors may govern the magnitude of coseismic temperature rise and thus dynamic weakening mechanisms that enable earthquakes to propagate on these thin slip surfaces.

## ■ BACKGROUND

## **Geologic Setting**

The Rio Grande rift is a zone of continental crustal extension that roughly parallels the Rocky Mountains from northern Colorado to Texas (Chapin and Cather, 1994; Keller and Baldridge, 1999). Extension initiated in the late Oligocene along the length of the Rio Grande rift, and this zone is considered to be active today (Chapin and Cather, 1994; Machette, 1998; Miggins et al., 2002; Landman and Flowers, 2013; Ricketts et al., 2014). The sedimentary record in the rift basins reflects rapid Miocene extension and topographic relief development along rift flanks (e.g., Cather et al., 1994; Ingersoll, 2001). Volcanism accompanying rifting peaked at ca. 28 Ma and continued episodically thereafter, including Pleistocene volcanism in New Mexico (Lipman and Mehnert, 1975; Chapin et al., 2004). Recent deformation in

the Rio Grande rift is recorded by active seismicity and strain (<1 mm/yr) from continuous global positioning system (GPS) site measurements (Berglund et al., 2012).

The Rio Grande rift in New Mexico is characterized by a series of linked half grabens bounded by rift shoulders and separated by transfer zones (Fig. 1A; Chapin and Cather, 1994; Lewis and Baldridge, 1994; Ingersoll, 2001; Ricketts et al., 2015). In central New Mexico, the Sandia Mountains make up the footwall of a large west-dipping, northstriking, normal fault delineating the eastern margin of the Rio Grande rift (Fig. 1B; Russell and Snelson,

1994; Ricketts et al., 2015). The Sandia Mountains are bounded on the north by the Placitas fault zone and on the south by the Tijeras fault zone (Kelley and Northrop, 1975). Here, the footwall exposes the ca. 1400 Ma Sandia granite (zircon U-Pb ages: 1437 ± 47 Ma [Steiger and Wasserburg, 1966]; 1453 ± 12 Ma [Holland et al., 2020]), which shares a similar rich and protracted tectonic history with most basement rocks in New Mexico (Kelley, 1977; Karlstrom et al., 1999a; Holland et al., 2020). The granite was emplaced into Paleoproterozoic metamorphic rocks of the Manzano Group, where the oldest units are dated between ca. 1680 and 1660 Ma, which is

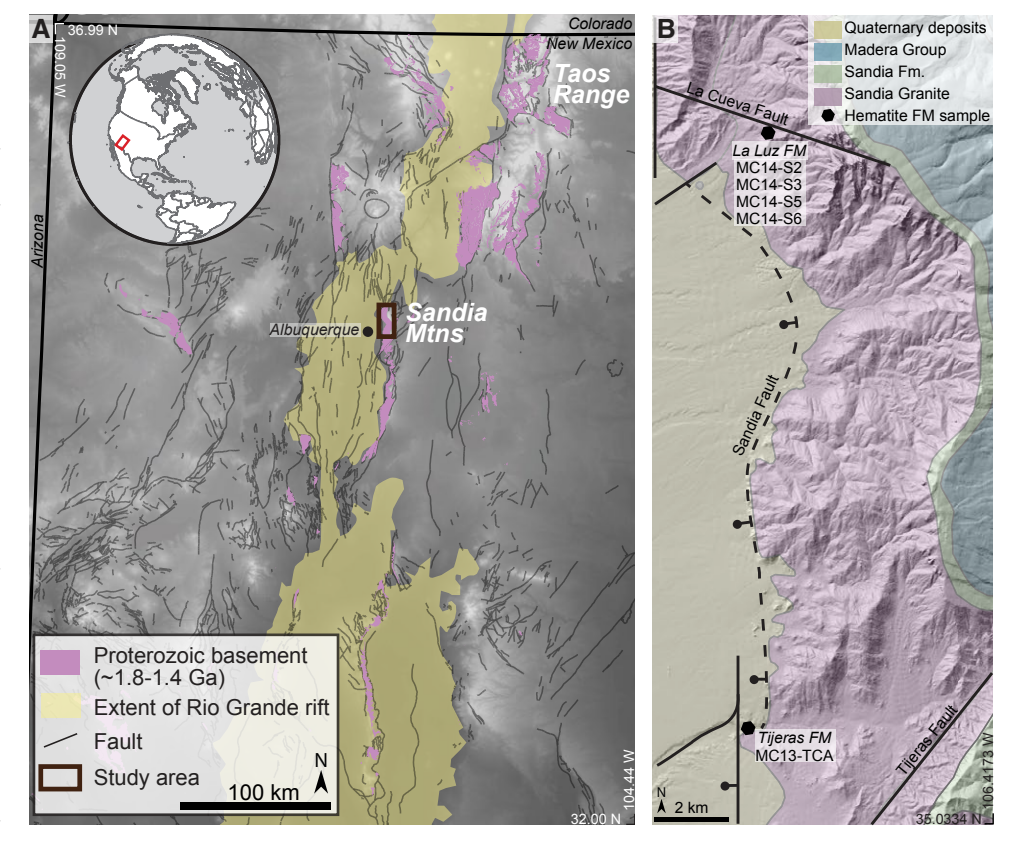


Figure 1. (A) Digital elevation model (DEM) of New Mexico highlighting distribution of Proterozoic basement, extent of Rio Grande rift-related sedimentary rocks and basins, and faults. Study area in the Sandia Mountains is denoted by the black box. (B) Simplified geologic map of the study area overlain on a shaded relief DEM with sample locations. FM—fault mirror.

part of the Mazatzal tectonic province (Kirby et al., 1995; Karlstrom et al., 2004; Holland et al., 2020). The Sandia granite and basement units collectively record regional tectonism of the Grenville orogeny (ca. 1300-1100 Ma) during formation of the Rodinian supercontinent (Mosher, 1998; Karlstrom et al., 1999a, 1999b, 2004). Bedrock 40Ar/39Ar thermochronologic data from the Sangre de Cristo Range of north-central New Mexico indicate regional cooling related to breakup of Rodinia at ca. 1000-800 Ma (Sanders et al., 2006). From ca. 800 to 320 Ma, extensive regional erosion created a regional nonconformity (Mallory, 1958; Karlstrom et al., 1999a). In the Sandia Mountains, this is represented by the Pennsylvanian Sandia Formation and Madera Group overlying Proterozoic basement (Kelley and Northrop, 1975; Krainer and Lucas, 2013). During the late Carboniferous to early Permian, the Ancestral Rocky Mountain orogeny caused local uplifts and sedimentary basins (Dickinson and Synder, 1978; Karlstrom et al., 1999a; Leary et al., 2020). The Late Cretaceous-early Cenozoic Laramide orogeny, characterized by basement-cored uplifts in north-central New Mexico, produced thrust faults on the eastern margin of the Sandia Mountains (Dickinson and Snyder, 1978; Cather et al., 2004). Normal faulting related to the Rio Grande rift generated the easttilted Sandia Mountains and topography seen today (Aldrich et al., 1986; Ricketts et al., 2015).

The Precambrian basement in the Sandia Mountains is cut by numerous faults that record middle- to upper-crustal deformation over the last ~1700 m.y. (Kelley and Northrop, 1975; Karlstrom et al., 1999a; Holland et al., 2020). Generally, NE-trending structures are interpreted to have originated in the Paleoproterozoic, reactivated during the Mesoproterozoic, influenced the geometry of Laramide structures, and acted as major transfer systems during Miocene Rio Grande rift extension (Abbott and Goodwin, 1995; Karlstrom et al., 1999a). NW-trending structures are interpreted to have originated in the Mesoproterozoic Grenville orogeny, reactivated and/ or originated during the Ancestral Rocky Mountain deformation, served as major contractional structures during the Laramide orogeny, and acted as minor transfer zones in Rio Grande rift extension. Laramide structures may have influenced basin and fault geometry of the Rio Grande rift (Karlstrom et al., 1999a; Ricketts et al., 2015). More broadly, the overall north-south trend of the Rocky Mountains and Rio Grande rift may be inherited from extension associated with the breakup of Rodina ca. 800 Ma (e.g., Timmons et al., 2001).

In this study, we focused on hematite-coated minor (square centimeter exposed surface area) faults that are collocated with the trace of range-scale fault zones. The La Cueva fault is one such structure; it is a NW-trending fault exposed in the Sandia granite (Fig. 1B; Kelley and Northrop, 1975; Read et al., 1999). The timing of initiation and extent of offset along the La Cueva fault are poorly constrained, and it may have originated in the Ancestral Rocky Mountains orogeny (Kelley and Northrop, 1975; Read et al., 1999; Abbott et al., 2004). The Sandia fault zone is the N-S-trending normal fault responsible for Rio Grande rift flank development and exhumation of the Sandia granite (Fig. 1B).

## **Hematite Microstructures in Fault Rocks**

Hematite formation is redox dependent. Iron mobility requires reducing conditions, and hematite precipitates from oxidizing fluids present in or circulating through higher-permeability faults and fracture networks, forming veins and thin coatings on fault surfaces (Cornell and Schwertmann, 2003; Ault, 2020). Hematite mineralization occurs over a range of fluid temperatures (<100-300 °C) and crustal depths (e.g., Cornell and Schwertmann, 2003; Dideriksen et al., 2007). Initial grain size and morphology are controlled by the fluid and ambient temperatures, as well as geochemistry (Catling and Moore, 2003). Fault rock hematite exhibits diverse textures and morphologies that reflect the thermal, geochemical, and stress state of mineralization and post-formation deformation (McDermott et al., 2017; Ault, 2020). Ault (2020) reviewed hematite occurrence, textures, and interpretations of deformation processes in fault rocks. Here, we highlight prior textural observations and frictional character istics relevant for our Sandia hematite fault mirrors.

Specular hematite occurs as micrometer-thick, elongate plates in fault veins and as a cement in

fault breccia (e.g., Ault et al., 2015; Jensen et al., 2018). Hematite deformation mechanisms have been investigated in coarse-grained, specular Fe ore, at high temperatures and pressures and low laboratory strain rates (e.g., Rosière et al., 2001; Siemes et al., 2003, 2008, 2010, 2011; Mendes and Lagoeiro, 2012; Rosière et al., 2013; Gonçalves et al., 2015; Ferreira et al., 2016). Specular hematite veins may serve as zones of weakness that localize subsequent deformation (e.g., McDermott et al., 2017). Hematite deformation experiments indicated that hematite is relatively weak (Siemes et al., 2003; Gonçalves et al., 2015; Calzolari et al., 2020). For example, friction experiments at ambient conditions and seismic slip rates (up to 0.32 m/s) showed relatively low coefficients of both quasi-static and dynamic friction ( $\mu \sim 0.28 \pm 0.12$ ; Calzolari et al., 2020). Deformation experiments at high temperature and pressure in polyphase rocks indicated that the presence of 2%-10% hematite causes dramatic strain weakening and localization (Gonçalves et al., 2015).

Some hematite slip surfaces that develop within coarse-grained specularite are characterized by cataclastic, subangular to subrounded hematite fragments that form from comminution during deformation (Ault et al., 2015; McDermott et al., 2017). Hematite fault mirrors may be composed of these cataclastic micron- to sub-micron-scale particles, but some instances also exhibit micrograins to nanograins with polygonal (triple-junction-forming) and/or lobate grain boundaries (Ault et al., 2015, 2019; McDermott et al., 2017). The distribution of these particle morphologies relative to the fault mirror surface can provide information about the thermally mediated dynamic weakening mechanisms. For example, polygonal grains that occur in micrometer-scale clusters at the fault mirror surface may reflect asperity flash heating (McDermott et al., 2017), and pervasive polygonal grains adjacent to the fault mirror surface may indicate grain growth following shear heating and associated melting (Ault et al., 2019). Deformation experiments at the lower end of seismic slip rates yielded localized fault mirror patches comprising sintered nanoparticles (Calzolari et al., 2020). These textures reflect the interplay between grain-size reduction and temperature rise during seismic slip on thin

fault surfaces (Ault et al., 2015; McDermott et al., 2017; Calzolari et al., 2020; Hirono et al., 2020).

# Hematite (U-Th)/He Thermochronometry in Fault Zones

Hematite He dates record the conditions of hematite mineralization and the postformation thermal, mechanical, chemical, and/or fluid-interaction history (Ault, 2020). The closure temperature  $(T_c)$ of the hematite He system is ~25-250 °C (assuming a 10 °C/m.y. cooling rate; Farley and Flowers, 2012; Evenson et al., 2014; Farley, 2018). Hematite, particularly in fault rocks, occurs as polycrystalline aggregates and exhibits polydomain diffusion, meaning each hematite crystal in the aggregate is a diffusion domain (Farley and Flowers, 2012; Evenson et al., 2014; Farley and McKeon, 2015; Farley, 2018). Hematite He  $T_c$  increases with domain (grain) size, so the  $T_c$  of a dated aliquot is controlled by the grain-size distribution of the polycrystalline material (Evenson et al., 2014; McDermott et al., 2017).

Because hematite is a secondary phase in faults that forms over a range of depths, it can precipitate either below or above its T<sub>c</sub> (Cornell and Schwertmann, 2003; Ault, 2020). This complexity, combined with conditions amenable to open-system behavior (i.e., He loss, or parent isotope loss/gain), means that hematite He dates from fault rocks may record the timing of mineralization, cooling due to tectonic or erosional exhumation, thermal resetting due to friction or hydrothermal fluids, or U addition (e.g. Reiners et al., 2014; Ault et al., 2015; McDermott et al., 2017; Moser et al., 2017; Wu et al., 2019). Discriminating between these possibilities requires multiscale hematite textural characterization, aliquot-specific  $T_c$ estimates from grain-size distribution measurements, evaluation of intrasample date patterns as a function of Th/U, and comparison between hematite He dates and the ambient thermal history from conventional low-temperature thermochronometry with complementary  $T_c$  (McDermott et al., 2017; Ault, 2020). For example, differences between hematite He data from samples with well-characterized deformation textures (see "Hematite Microstructures in Fault Rocks" section) and apatite (U-Th)/He (apatite He) and/or apatite fission-track (AFT) thermochronometry can bracket the ambient temperature and thus depths of hematite formation, cooling, and/or fault slip.

## SAMPLES AND METHODS

A suite of hematite fault mirrors, with underlying vein and/or cataclasite, cuts the Sandia granite and is collectively exposed in the uplifted rift flank adjacent to the Albuquerque Basin (Fig. 1). Three hematite fault mirrors (MC14-s2, MC14-s3, MC14-s5) and one Sandia granite host rock sample (MC14-s6) were collected from within the mapped trace of the La Cueva fault zone along the wellknown La Luz trail in NE Albuquerque and the same sampling transect of House et al. (2003) (Fig. 1B). Hereafter, we refer to these samples informally as the "La Luz" hematite fault mirrors. One hematite fault mirror with underlying vein/cataclasite sample (MC13-TC) was collected from Tijeras Wash in the vicinity of the Sandia fault zone, and we refer to this sample as "Tijeras" (Fig. 1B). The La Luz and Tijeras fault mirrors were targeted for scanning electron microscopy (SEM)-based microstructural and hematite He thermochronometry analyses.

Hematite aliquots were isolated using a Dremel™ tool by first drilling below and undercutting the target hematite material, which was subsequently broken off of the sample. Sample chips were then wrapped in paper and gently disaggregated with a hammer. Aliquots were hand selected, avoiding pieces with evidence of tool marks, using fine-point tweezers (Fig. S1¹). Microstructural analyses were conducted on samples representative of dated material in plan and cross-section views relative to the fault mirror surface via secondary electron (SE) and backscatter electron (BSE) SEM using an FEI Quanta 650 Field Emission SEM at Utah State University's Microscopy Core Facility. Energy-dispersive spectroscopy (EDS) was conducted on a subset of samples to provide

first-order constraints on major-element chemical variations in the fault mirror volume. Grain-size distributions were measured from SEM images with ImageJ software at and away from the slip surfaces (Abràmoff et al., 2004). Relative abundances of hematite and host rock were quantified from BSE SEM images using ImageJ software.

The He, U, and Th contents of target thermochronometry aliquots were measured at the Arizona Radiogenic Helium Dating Laboratory at the University of Arizona using standard apatite lasing temperatures (~900-1050 °C) to prevent U and Th volatilization and zircon dissolution procedures. Method details are provided in the supplemental text (see footnote 1). We evaluated U loss during He degassing, which would result in anomalously old dates, using intrasample date versus Th/U patterns (Fig. S2; Vasconcelos et al., 2013). We did not apply an alpha ejection correction to our dates because we assumed He loss was balanced by He implantation (Farley and Flowers, 2012). Fault mirror aliquots came from slip surfaces localized within specular hematite veins, and thus the opposing side of the fault mirror is likely hematite (e.g., Figs. 2C and 2D). Aliquots from the fault mirror volume and underlying cataclasite were located away from the hematite-granite contact by several times the α-stopping distance, or the distance over which a high-energy  $\alpha$  particle (He) comes to rest in solid matter (Fig. S1; Farley et al., 1996).

## RESULTS

## **Field Observations**

The Sandia granite that hosts the hematite fault mirrors is a porphyritic granite comprised of quartz, plagioclase, biotite, and K-feldspar with <5-cm-diameter feldspar phenocrysts. Along the La Luz trail, the granite exhibits zones of millimeter- to centimeter-thick cataclasite with Fe-oxide alteration that appear to follow the approximate trend of the La Cueva fault (approximately NW-SE). Here, hematite fault mirrors are oriented oblique to orthogonal with respect to specular hematite veins and cataclasites, which are typically <10 cm thick (Fig. 2B).

<sup>&</sup>lt;sup>1</sup>Supplemental Material. Detailed microscopy and thermochronology methodologies, (U-Th)/He data tables, grain size measurements, thermal history model input table, and figures. Please visit <a href="https://doi.org/10.1130/GEOS.S.16679530">https://doi.org/10.1130/GEOS.S.16679530</a> to access the supplemental material, and contact editing @geosociety.org with any questions.

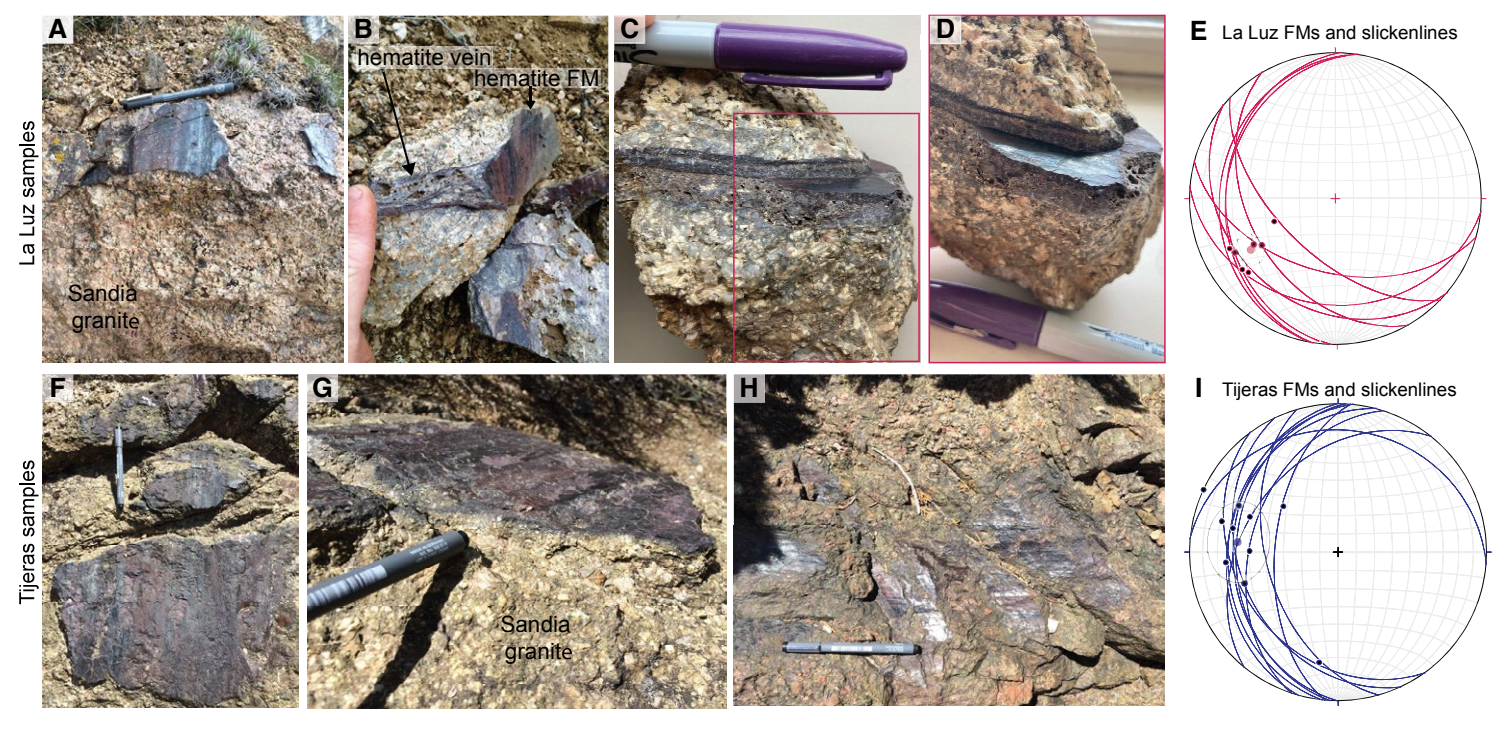


Figure 2. Field and hand sample photos of high-gloss, hematite fault mirrors (FMs) with local iridescence and slickenlines, and stereonets showing fault plane and slickenline orientations: (A–E) La Luz samples, (F–I) Tijeras samples. (E, I) Stereonet plots of fault mirror (planes) and slickenline (lines) orientations with mean orientations (colored points). Stereonets were plotted using the Stereonet program (Allmendinger et al., 2013; Cardozo and Allmendinger, 2013).

In Tijeras Wash, roughly E-W-trending zones of chlorite and Fe-oxide alteration have local specular hematite and quartz veins. The hematite fault mirrors are collocated with this alteration and zones of cataclasite (<10 cm thick).

Hematite fault mirrors from both localities are high-gloss, light-reflective, and locally iridescent surfaces with metallic luster (Figs. 2A–2H). Material defining the fault mirror appears to have millimeter thickness at the field scale. The fault mirror volume is underlain by a millimeter- to centimeter-thick zone of hematite-cemented cataclasite (Fig. 2). The underlying granite is locally deformed and exhibits some grain-size reduction, with micrometer- to millimeter-diameter quartz and feldspar grains adjacent to hematite-cemented cataclasite and the fault mirror surface. Although hematite

fault mirrors are co-located with and crosscuts the hematite-cemented cataclasite, it is never cut by or incorporated into the cataclasite (Figs. 2B and 2C).

Fault mirror surfaces are corrugated on a centimeter scale and exhibit sets of slickenlines displaying one or more orientations, with the dominant slickenline orientation parallel to the axis of the corrugations (Figs. 2A, 2G, and 2H). La Luz fault mirrors generally strike NW-SE, with a mean strike and dip of 140/30°SW (Fig. 2E). The mean orientation of slickenlines on these slip surfaces is 32→239°, recording dominantly dip-slip motion (Fig. 2E). Tijeras fault mirror orientations are variable, but they dominantly strike ~185 and dip 30°–50°W (average of fault planes 185/32°E; Fig. 2I), similar to the orientation of the Sandia fault (Figs. 1 and 2I). The Fisher mean vector of the slickenlines

is 32 $\rightarrow$ 276°, indicating dominantly dip-slip motion along the faults (Fig. 2I).

## **Hematite Fault Mirror Microstructures**

In La Luz fault mirrors, hematite occurs in two microstructural domains: in a layer at the slip surface, referred to as the "fault mirror volume" (domain 1), and in underlying cataclasite (domain 2). Domain 1 is nearly pure hematite in all samples (±quartz and feldspar, presumably derived from the Sandia granite). Domain 2 contains varying proportions of hematite and host rock between samples (Fig. 3).

Sample MC14-s2 consists of an ~8–15-µm-thick domain 1 with ~69% hematite and ~31% rounded to subrounded quartz fragments (Figs. 3A and 4).

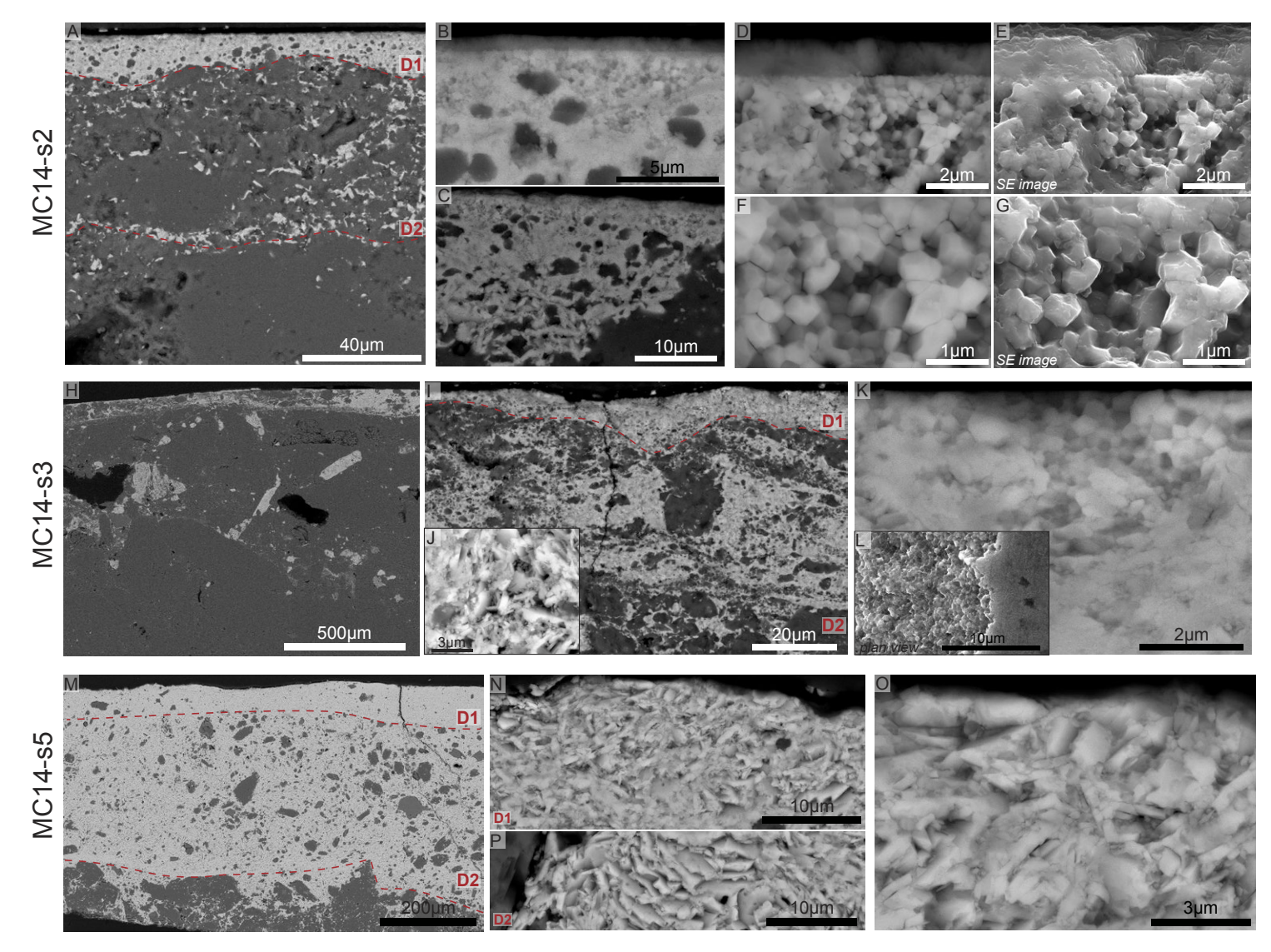


Figure 3. Scanning electron microscope (SEM) backscattered electron (BSE) images of La Luz samples at various scales showing fault surface and hematite textures in domain 1 (D1, fault mirror volume) and domain 2 (D2, cataclasite): (A–G) sample MC14-s2, (H–L) sample MC14-s3, and (M–P) sample MC14-s5. Light-gray regions are hematite, and dark-gray regions in images are dominantly quartz and feldspar. Images E and G are complementary secondary electron (SE) images to images D and F, respectively. Inset image J shows cataclasite and nanoparticles from D1, and image L shows the smooth fault mirror surface in plan view (right side of image) with underlying polygonal grains.

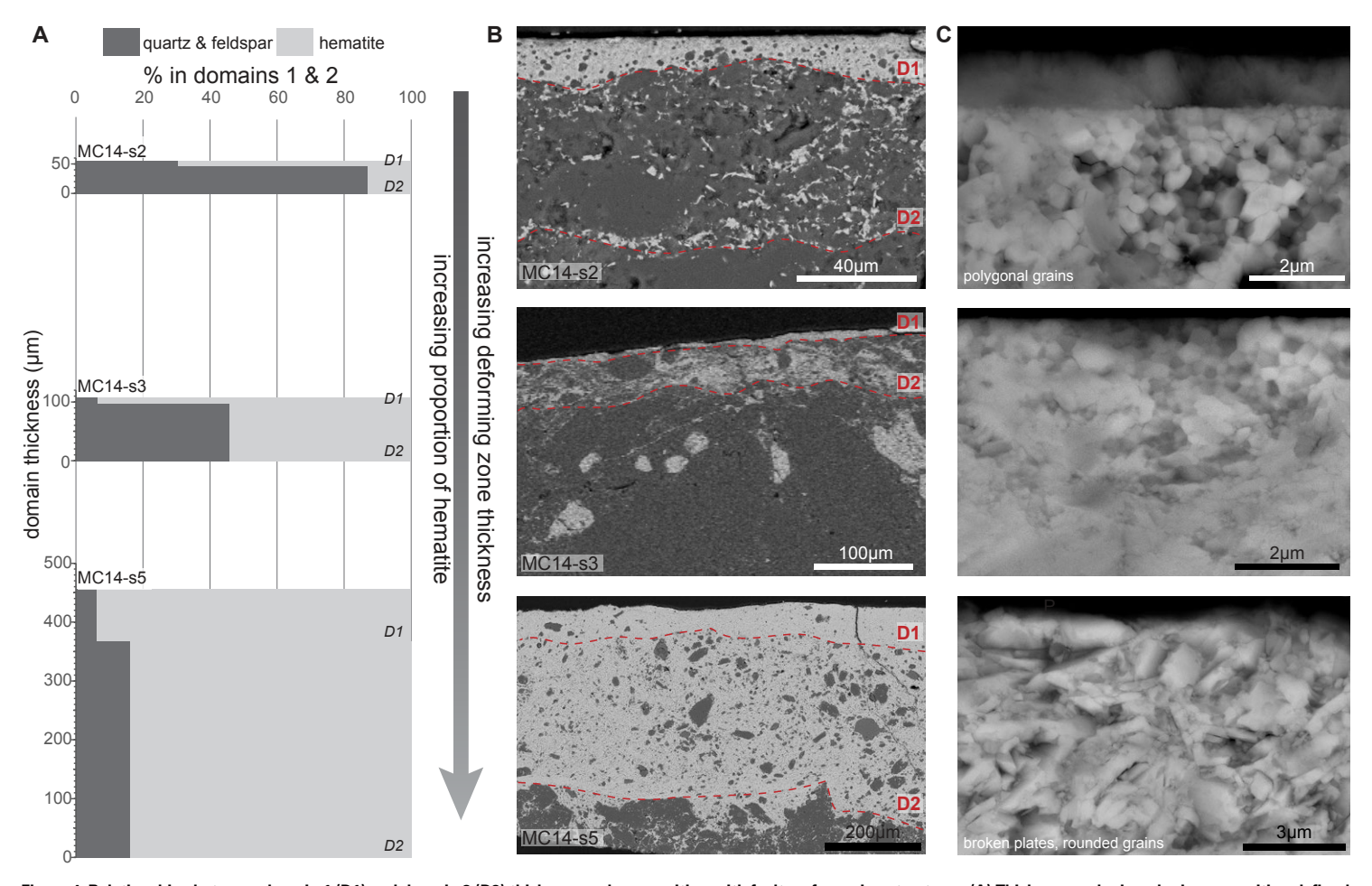


Figure 4. Relationships between domain 1 (D1) and domain 2 (D2) thickness and composition with fault surface microstructures. (A) Thickness and mineralogic composition defined by proportions of hematite (light gray) and quartz and feldspar particles (dark gray). (B) Scanning electron microscope (SEM) backscattered electron (BSE) images of domains 1 and 2. Light-gray regions are hematite, and dark-gray regions in images are dominantly quartz and feldspar. Note the different scales. (C) SEM BSE images of domain 1 microstructures at the slip surface at similar scales.

Domain 1 includes an ~2.5–5-µm-thick layer of polygonal hematite grains at the fault mirror surface (Figs. 3B–3G). Polygonal crystals exhibit triple-junction grain boundaries, appear sintered (cf. Hirono et al., 2020), and lack shape preferred orientation (Figs. 3F and 3G). The radius of these grains is 0.06–0.22  $\mu$ m, with a mean of 0.12  $\mu$ m. High-resolution EDS data indicate that these grains

contain trace Si (~1%) (Fig. S3). Polygonal grains are underlain by cataclastic hematite characterized by broken plates and subrounded nanoparticles, which grade into whole plates away from the fault mirror surface (Fig. 3C). Polygonal grains are overlain by an ~0.6–1.0-µm-thick, featureless "film," which lacks discernible grains or grain boundaries at the micrometer and sub-micrometer SEM scale (Figs. 3B,

3D, and 3E). This film is composed of O, Fe, Si, AI, CI, and P (~47%, 44%, 5%, 3%, 0.5%, and 0.5% respectively; Fig. S3). The boundary with the underlying polygonal hematite grains is distinct. Domain 2 is ~40–50  $\mu$ m thick and dominantly quartz and feldspar (~87%) with local hematite plates (~13%) (Figs. 3A and 4). Hematite plate half-widths in domain 2 are 0.09–0.53  $\mu$ m, with a mean of 0.25  $\mu$ m.

Sample MC14-s3 has an ~65-120-µm-thick, hematite-rich deformed zone above comparatively undeformed granite with some hematite (Figs. 3H-3I). Domain 1 is  $\sim$ 5-10  $\mu$ m thick and  $\sim$ 93% hematite and 7% quartz and feldspar (Figs. 3I and 4). Domain 1 has an ~2-2.5-µm-thick layer of sintered polygonal hematite grains at the fault mirror surface, observed both in cross-section and plan views (Figs. 3K and 3L). Polygonal grains grade into subangular to subrounded nanoparticles away from the fault mirror surface (Fig. 3J). The radius of domain 1 grains is  $0.05-0.21 \mu m$ , with a mean of  $0.11 \mu m$ . The smallest polygonal grain is larger than the largest grains in the underlying cataclasite within 5 µm of the slip surface (Fig. 3K). Domain 2 is ~65-100 µm thick (Fig. 3I), with comminuted, subrounded hematite grains and broken hematite plates (Figs. 31-3J). The hematite grain radius and/or plate half-width in domain 2 are 0.08-0.65 µm, with a mean of 0.21 um. Domain 2 is ~45%-62% hematite and ~38%-55% guartz and feldspar. In plan view, the slip surface appears smooth and nearly featureless at the SEM scale with some localized slickenlines (Fig. 3L).

Sample MC15-s5 has an ~68–88-µm-thick domain 1 of nearly pure hematite (~94%) with lesser subangular to subrounded quartz fragments (~6%) below an undulatory fault mirror surface (Figs. 3M and 4). Domain 1 hematite occurs as broken plates and subrounded hematite grains, with radii/plate half-width of 0.05–0.19 µm and mean of 0.11 µm (Figs. 3N–3O). Domain 2 is ~350–370 µm thick and contains dominantly hematite plates (~84%) with quartz fragments (~16%) (Figs. 3M and 3P). The hematite plates have half-widths of 0.19–0.69 µm and a mean of 0.39 µm. Domain 2 is underlain by granite cataclasite with interstitial hematite plates (Fig. 3M).

The Tijeras hematite fault mirror is characterized by multiple internal slip surfaces. Associated, texturally asymmetric deformation zones are ten to hundreds of micrometers thick and lack the domain structure of the La Luz samples (Figs. 5A and 5C). For example, one imaged chip or subsample from MC14-TCA has two internal deformation zones; one is ~120 µm thick (slip surface 1 in Fig. 5A) with an ~200-µm-thick slip zone below it (slip surface 2 in Fig. 5A). The slip surfaces within these zones are delineated by nearly pure hematite (Figs. 5B

e/article-pdf/18/1/241/5515844/241.pdf

and 5D) and are underlain by hematite-rich cataclasite with deformed Al-Mg-rich clays (Figs. 5C and 5D). Slip surface hematite occurs as ~0.1-µm-radius rounded grains (0.05–0.29 µm; mean 0.11 µm) that locally appear sintered and lesser broken plates. Hematite in the underlying cataclasite occurs only

as plates (Fig. 5B), with half-widths of 0.09–0.63  $\mu m$  and a mean of 0.23  $\mu m$ . The contact between the top cataclasite domain and lower slip surface 2 is sharp, with truncated quartz and feldspar grains (Fig. 5C) and rounded, sintered hematite grains (Figs. 5C and 5D). The rounded hematite grains

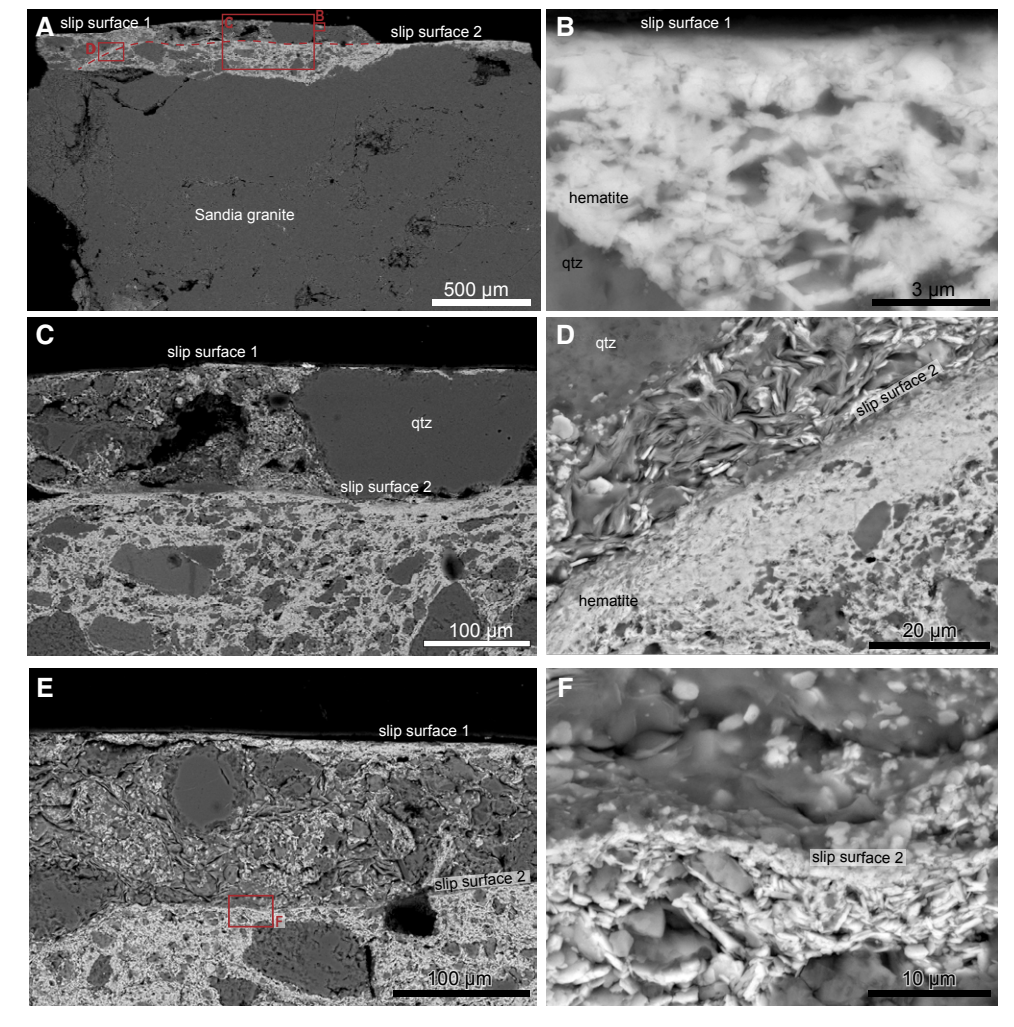


Figure 5. Scanning electron microscope (SEM) backscattered electron (BSE) images of Tijeras sample (MC13-TCA) at various scales showing multiple slip surfaces (A, C, E) and their related slip surface microstructures (B, D, F); qtz—quartz. Locations of images B, C, and D are shown on image A (red boxes), and location of image in F is shown on image E.

that define slip surface 2 grade into underlying broken hematite plates. The basal contact between the hematite-rich cataclasite and underlying largely undeformed Sandia granite is sharp but undulatory.

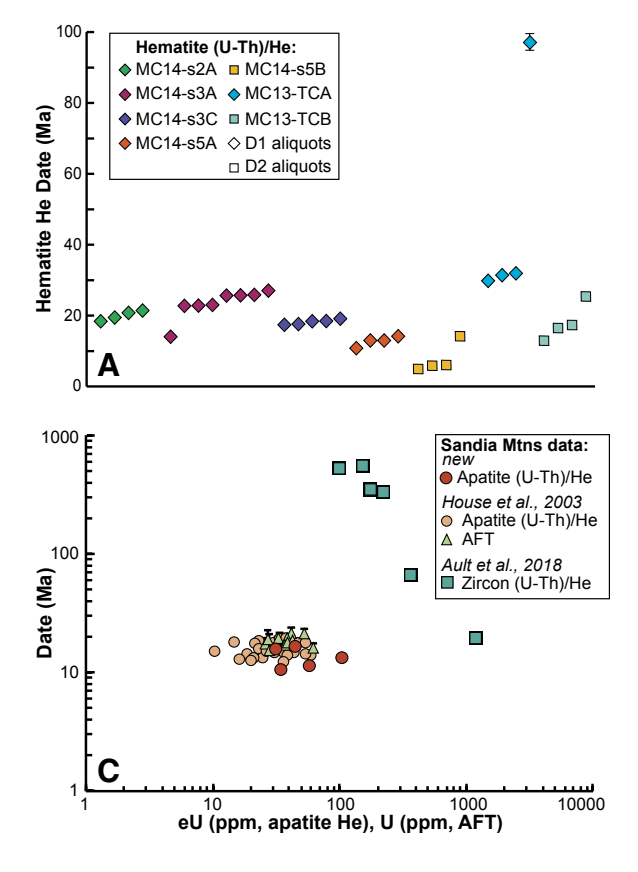
## (U-Th)/He Thermochronometry Results

We report 33 new hematite He dates from the fault mirror volume of five fault mirrors and associated underlying hematite-cemented cataclasite from two of these fault mirrors (Fig. 6A; Fig. S1; Table S1 [footnote 1]). We also acquired new apatite He data from a Sandia granite sample adjacent to the La Luz hematite fault mirrors (Fig. 6B; Table S2). We compare these bedrock data with previously

published zircon He results from the same sample and apatite He and AFT thermochronometry from nearby sites along the La Luz trail (Fig. 6C; Table S3; House et al., 2003; Ault et al., 2018). The (U-Th)/He dates are reported as the geometric mean with  $1\sigma$  standard deviation of the mean or as the range of single-aliquot dates with their  $2\sigma$  analytical uncertainty if the standard deviation of the mean was >20% (Flowers and Kelley, 2011). Hematite fault mirror samples names ending in "A" and "C" are aliquots isolated from the fault mirror volume (domain 1) and those ending in "B" are aliquots from underlying cataclasite (domain 2).

Individual aliquot hematite He dates range from  $97.1 \pm 2.4$  Ma to  $4.9 \pm 0.2$  Ma across the data set (Fig. 6A; Tables S1 and S4). Over 80% of the

hematite He dates fall between ca. 25 and 10 Ma. Analyses from domain 1 of the La Luz samples yield mean dates of 23.4 ± 4.1 Ma with Th/U of 0.09-0.37 (MC14-s3A; n = 8),  $18.2 \pm 0.7$  Ma with Th/U of 0.26-0.43 (MC14-s3C; n = 5), and 20.1  $\pm$  1.4 Ma with Th/U of 0.26-0.36 (MC14-s2A; n = 4; one aliquot is excluded based on a high Th/U of 0.97, suggesting U volatilization during degassing; Fig. S2). The mean hematite He date from sample MC14-s5A is  $12.8 \pm 1.4$  Ma with Th/U of 0.31-0.56(n = 4), and single-aliquot dates from MC14-s5B are  $14.2 \pm 0.2$  Ma to  $4.9 \pm 0.1$  with Th/U of 1.02-1.29(n = 4). Tijeras sample MC13-TC yielded singlealiquot hematite He dates of 97.1 ± 1.2 Ma to 29.8  $\pm$  0.4 Ma with Th/U of 1.32–1.68 (MC13-TCA; n = 4) from the fault mirror volume and 25.5 ± 0.3 Ma to



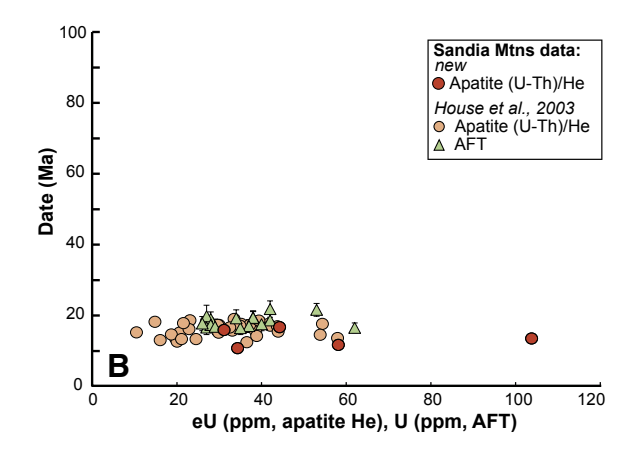


Figure 6. Low-temperature thermochronology data. (A) Hematite (U-Th)/He (He) dates for individual aliquots classified by sample with 2 $\sigma$  analytical error (error bars within the symbols). (B) Apatite He and apatite fission-track (AFT) dates as a function of effective U (eU). (C) Apatite He, AFT, and zircon He dates as a function of effective U (eU) from the Sandia granite in the Sandia Mountains (note the log scale of the y axis).

13.0  $\pm$  0.2 Ma with Th/U of 3.24–4.56 (MC13-TCB; n = 4) from the cataclasite.

The mean apatite He date from Sandia granite sample MC14-s6 is  $13.6 \pm 2.6 \text{ Ma}$  (n = 5). Individual aliquot dates are uniform over the measured effective U (eU) range of 31-102 ppm (Fig. 6B). This new date overlaps with published apatite He and AFT data from House et al. (2003) and Abbott et al. (2004) (Fig. 6C). For example, mean AFT and He dates from a La Luz trail transect of House et al. (2003) range from 21.7 ± 2.3 Ma to 16.3 ± 1.8 Ma and 18.5 ± 1.3 Ma to 12.9 ± 0.9 Ma, respectively. Published AFT dates from the Sandia granite in the footwall of the Tijeras fault exposed in Tijeras Wash near Golden, New Mexico, were 24.9 ± 2.4 Ma and 21.4 ± 3.3 Ma (Abbott et al., 2004). Zircon He results from sample MC14-s6 are reported in Ault et al. (2018) and are summarized here. Individual aliquot dates range from 555 ± 16 Ma to  $19.5 \pm 0.6$  Ma (n = 6). Data define a subtle positive date-eU relationship between ca. 555-526 Ma and 100-152 ppm eU and a strong negative trend from ca. 345 to 20 Ma and 166-1175 ppm eU (Fig. 6C).

## COMPARISON BETWEEN HEMATITE AND CONVENTIONAL THERMOCHRONOMETRY

We compared our hematite He dates and grainsize-dependent T<sub>c</sub> with apatite He and AFT dates and nominal  $T_c$  from the nearby Sandia granite (Fig. 7). This aided the first-order interpretations of our hematite He dates, potentially shedding light on whether they record a fault slip-related process such as mineralization or thermal resetting due to frictional heating, or ambient cooling due to exhumation (e.g., Ault et al., 2015; McDermott et al., 2017; Ault, 2020). We bracketed the hematite He  $T_c$  for each sample by measuring the diameter or plate thickness of >50 grains from representative, cross-sectional SEM BSE images and calculating the range and mean  $T_c$ values for each sample using the equation of Dodson (1973) and hematite diffusion kinetics of Farley (2018). Using diffusion kinetic parameters of Farley and Flowers (2012) and Evenson et al. (2014) did not substantively change the  $T_c$  estimates (Fig. S4). Results of grain-size measurements and calculated

 $T_{\rm c}$  values are summarized in Table S4. The minimum and maximum  $T_{\rm c}$  values across all samples are 74 °C to 109 °C. The domain 1/fault mirror volume  $T_{\rm c}$  values are 75–108 °C with mean  $T_{\rm c}$  of ~88 °C. Domain 2/cataclasite hematite had a  $T_{\rm c}$  of 82–109 °C with mean  $T_{\rm c}$  of ~98 °C.

Nearly all hematite He dates overlap with new and published regional apatite He and AFT data and zircon dates from high-eU grains (Kelley et al., 1992; Abbott et al., 2004; House et al., 2003; Ricketts et al., 2015; Ault et al., 2018). Domain 1 samples MC14-s3A, MC14-s3C, MC14-s2A, MC14-s5A, and MC13-TCA (1) have a mean  $T_c$  that falls between the  $T_c$  for apatite He and AFT (Gallagher et al., 1998; Flowers et al., 2009), and (2) yield similar hematite He dates of ca. 25-10 Ma to the conventional thermochronometry dates (Figs. 6A, 6B, and 7). This relationship suggests that this hematite formed at depth prior to or during inception of the Rio Grande rift, and that hematite He dates record ambient cooling through ~110-75 °C at ca. 25-10 Ma. We considered these scenarios further using thermal history forward models. The oldest individual aliquot date of 97.1 ± 2.4 Ma from sample MC13-TCA supports some hematite forming prior to the Miocene. This sample

showed evidence of multiple internal slip surfaces, and hematite He dates ranging from ca. 97 Ma to ca. 30 Ma may reflect multiple phases of hematite mineralization together with the postmineralization thermal history. We evaluated potential mineralization ages with thermal history modeling.

The underlying domain 2 hematite in samples MC14-s5B and MC13-TCB has higher mean  $T_c$  than domain 1, and hematite He dates also overlap with apatite He and AFT results from the host rock. However, hematite He dates from each of these samples are younger than dates from their corresponding domain 1 (MC14-s5A and MC13-TCA, respectively). This pattern is opposite to the expected trend given the larger grain size and thus higher  $T_c$  in domain 2. Aliquots from MC14-s5B consist of void spaces and large nonretentive (with respect to He) phases like quartz, presumably derived from the host rock during fault slip (Fig. 3M). Cataclasite from MC13-TCB similarly contains nonretentive phases (Fig. 5). The presence of these nonretentive phases can lead to non-thermally controlled He loss and may explain why observed hematite He dates are younger than their respective finer-grained fault mirror volume dates. For this reason, dates from

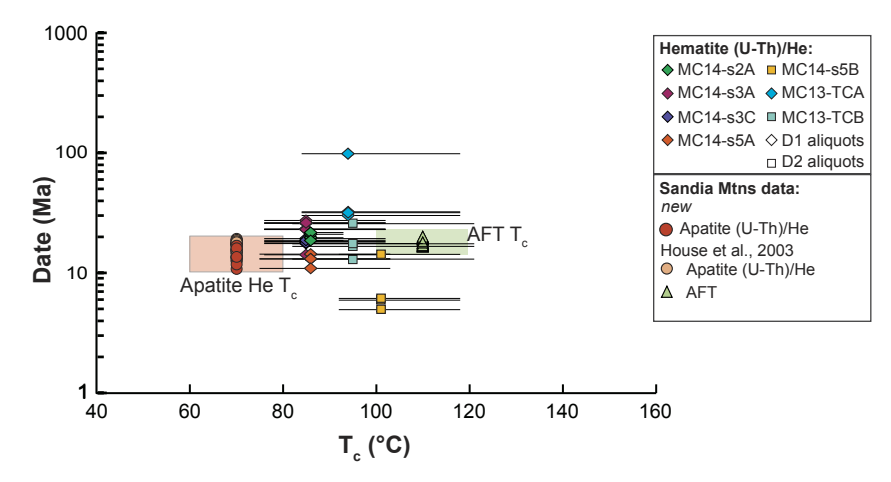


Figure 7. Apatite (U-Th)/He (He), apatite fission-track (AFT), and hematite He dates ( $1\sigma$  errors plotted smaller than symbols) related to their relative closure temperatures ( $T_c$ ). Hematite  $T_c$  values are plotted as the calculated mean with bars showing full range of  $T_c$  based on their grain-size distributions. Boxes represent the nominal  $T_c$  for apatite He (orange) and AFT (green).

samples MC14-s5B and MC13-TCB are not considered in the discussions below.

## THERMAL HISTORY MODELING

## Forward Model Framework

We built on our data comparison that suggested the hematite He dates record ambient cooling and employed a two-phase modeling approach to further interpret our hematite He dates. To do this, we first constructed a suite of thermal history models (i.e., "forward models"; Fig. 8A) that were consistent with observed apatite and zircon He date-eU trends and AFT dates, and then we used this time-temperature (t-T) model to predict hematite He dates over a range of grain sizes (Fig. 8). A secondary goal of the thermal modeling was to evaluate when the hematite first mineralized.

The thermal history modeling was conducted using HeFTy (Ketcham, 2005). For our first suite of models, we used the available radiation damagediffusivity kinetics for apatite (RDAAM; Flowers et al., 2009) and zircon (ZRDAAM; Guenthner et al., 2013) and AFT annealing kinetics of Ketcham et al. (2007). Forward thermal history models were based on, and slightly modified from, the thermal history model of Ault et al. (2018), which leveraged the zircon He date-eU trends and published apatite

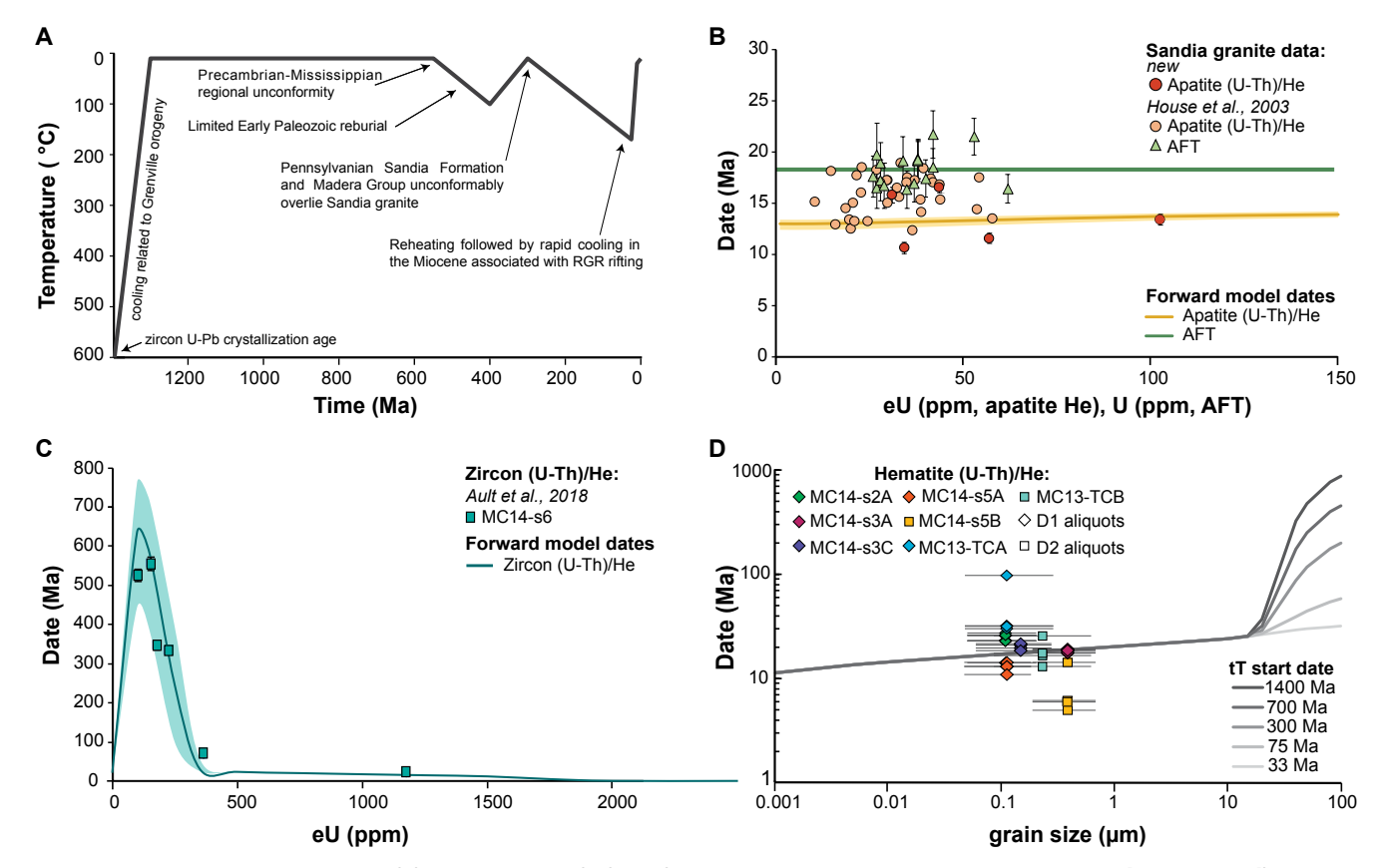


Figure 8. Thermal history modeling results. (A) Time-temperature (t-T) path (modified from Ault et al., 2018; see Table S5 for details [text footnote 1]). RGR-Rio Grande rift. (B) Apatite (U-Th)/He (He; orange line) and apatite fission-track (AFT; green line) model predicted vs. observed dates from this study and House et al. (2003). Forward model predicted dates over a range of effective U (eU) values are represented as lines with error envelopes that correspond to ±2σ of mean grain size for sample MC14-s6. (C) Zircon He model predicted (blue curve) vs. observed dates. Observed data and models are modified from Ault et al. (2018). (D) Hematite He forward model predicted dates (gray lines) as function of grain size for five different starting dates (mineralization ages). Observed hematite He dates are plotted as symbols at the mean grain size with bars representing the range of grain sizes.

He and AFT dates. The modeled t-T path included basic elements of the geologic history (Table S5), including rapid cooling at ca. 1400 Ma after pluton emplacement (Kirby et al., 1995), residence at near-surface conditions in the Mesoproterozoic and Neoproterozoic, minor early Paleozoic heating from burial (Kelley and Northrop, 1975), cooling to near-surface conditions evident by Pennsylvanian rocks unconformably overlying the granite (Kelley and Northrop, 1975; Krainer and Lucas, 2013), and Mesozoic and Cenozoic heating to ~170 °C followed by cooling related to Miocene rifting (Fig. 8A; House et al., 2003; Ricketts et al., 2015). Forward models used this t-T path to predict apatite and zircon He dates for a range of eU values using the mean apatite and zircon grain sizes  $\pm 2\sigma$  from sample MC14-s6 (Figs. 8B and 8C, solid line and transparent envelope, respectively). We compared the predicted apatite He and zircon He date-eU curves for sample MC14-s6 to previously published apatite He and AFT dates from House et al. (2003) (Fig. 8B).

We then used this t-T path to predict hematite He dates as a function of grain size because the dominant control on He diffusion, hematite  $T_c$ , and thus date, is the diffusion domain length scale (Farley and Flowers, 2012; Evenson et al., 2014; Farley and McKeon, 2015; Balout et al., 2017; Farley, 2018). We considered five different formation ages: 1400, 700, 300, 75, and 33 Ma, corresponding to possible hematite mineralization at ca. 1400 Ma associated with the emplacement of the Sandia granite (Kirby et al., 1995; Holland et al., 2020), at ca. 700 Ma similar to hematite mineralization in granitic basement in Colorado (Jensen et al., 2018), at ca. 300 Ma associated with pervasive fluid flow during the Ancestral Rocky Mountain orogeny (Geissman and Harlan, 2002), at ca. 75 Ma during the early Laramide orogeny (e.g., Karlstrom et al., 1999a), and at ca. 33 Ma associated with Oligocene extension and magmatism (House et al., 2003; Ricketts et al., 2015). Forward models were conducted using hematite diffusion kinetics of Farley (2018), and the assumed diffusion domain length scale was equivalent to grain radius or plate halfwidth (Farley, 2018; Jensen et al., 2018). Additional model parameters are detailed in the Supplemental

Material (Table S5 following the reporting protocol of Flowers et al., 2015).

### Model Outcomes

The predicted apatite He, AFT, and zircon He dates match the observed data patterns for each system and constrain the long-term t-T history to first order (Figs. 8B and 8C). For example, the predicted apatite He date-eU pattern involves uniform dates regardless of eU, broadly overlapping with data from sample MC14-s6 and the younger published apatite He dates of House et al. (2003) (Fig. 8B). The predicted zircon He date-eU patterns match the observed dates with a modeled positive relationship between <150 ppm eU and dates up to ca. 714 Ma and a strong negative relationship from ~150 to 2000 ppm eU with dates from ca. 714 to 1 Ma (Ault et al., 2018) (Fig. 8C). We note that the observed apatite He, AFT, and zircon He dates exhibit second-order dispersion around the model predictions, which can be attributed to disparate sample localities in different structural levels within the Sandia block and/or intrasample variations in diffusivity and annealing kinetics due to complexities not captured by the damage-diffusivity and annealing models (cf. Flowers and Kelley, 2011).

The predicted hematite He dates generally overlap with the observed date range, suggesting that these dates record rapid cooling through ~110-75 °C (Figs. 8A and 8D). Regardless of the model starting date, all five models yield identical predicted hematite He dates for grain radius/plate half-width <20 μm (Fig. 8D). All analyzed polycrystalline hematite aliquots have individual plate thicknesses between 0.1 and 1 µm. The models reveal that our observed hematite He dates are insensitive to the original mineralization age because Cenozoic reheating temperatures exceeded the aliquot  $T_c$  at observed grain sizes. Predicted dates diverge at grain sizes >20 µm and vary depending on the prescribed mineralization date (i.e., model start date; Fig. 8D). This indicates that undeformed hematite plates with thicknesses >20 µm could be targeted to constrain the timing of mineralization, which may be as old as the Mesoproterozoic or as young as ca. 33 Ma, associated with early Rio Grande rift fault activity and/or magmatism. Model outcomes also show that, for this thermal history, the distribution of grain sizes within domain 1 of our aliquots would need to vary by several orders of magnitude outside of what is observed to yield dates older than 33 Ma.

Comparisons between the observed hematite He dates and those predicted from our thermal history derived from new and previously published conventional thermochronometry data support a cooling age interpretation for most of our hematite dates. However, comparisons also reveal additional hematite He date complexity. For example, although hematite He dates from samples MC14-s2A and MC14-s3C are highly reproducible and consistent with predicted dates (Fig. 8D), samples MC14-s3A and MC13-TCA yield older dates than expected from the model. This is inconsistent with observed grain-size distributions of targeted domain 1 material or even the largest plates observed within these samples (i.e., the largest plate half-width is much less than 20 µm). These data patterns suggest that some aliquots have maintained a memory of their prepeak Cenozoic reheating He budget. Additionally, sample MC14-s5A yields dates younger than the predicted model (Fig. 8D), providing evidence for nonmonotonic processes inducing He loss at temperatures at or below the hematite  $T_c$ .

#### DISCUSSION

## Evidence of Strain Localization, Fault Reactivation, and Elevated Fault Slip Temperatures

Structural, field, and textural relationships support the interpretation that fault mirrors preferentially developed within preexisting specular hematite within the Sandia granite. In the La Luz samples, hematite fault mirrors are collocated with hematite-rich veins and millimeter- to centimeter-thick zones of hematite-cemented cataclasite (Figs. 2A–2D). The fault mirror surface-perpendicular textures grade from equant, polygonal, and locally sintered hematite grains or sub-micrometer- to

micrometer-scale cataclastic hematite particles in domain 1 to fractured and unbroken hematite plates in domain 2 (e.g., Fig. 3). In addition, the relative abundance of nonhematite grains, such as quartz and feldspar, which were presumably derived from the underlying granite during fault slip, generally increases away from the slip surface (Figs. 3C, 3J, and 4). Domain 1 material is not observed within or cut by domain 2 (Figs. 2B–2C). We infer these relationships to reflect progressive strain localization within preexisting hematite culminating in fault mirror development.

SEM images of the Tijeras fault mirror reveal internal slip surfaces that may reflect multiple zones of localized slip within comparatively weak, hematite-rich areas in the granite during a single slip event or several, sequential (?) episodes of deformation. Each slip surface shows evidence for strain localization along zones of hematite mineralization characterized by neoformed hematite plates that grade into nanometer-scale, sintered, rounded hematite grains (Figs. 5B, 5D, and 5F). The presence of neoformed plates below and associated with each slip interface suggests that fault surfaces may have developed during or after separate mineralization events, supporting fault reactivation. Individual hematite He dates of ca. 97 Ma to ca. 30 Ma from this sample also support multiple episodes of mineralization and deformation. It is likely that most hematite fault mirrors in our sample suite accommodated multiple slip events, as some La Luz fault mirrors have slickenlines with more than one orientation.

We suggest that these patterns of strain localization reflect the strength contrast between the hematite and the granitic host rock. Hematite has a quasi-static and dynamic coefficient of friction of ~0.4–0.2 (Calzolari et al., 2020), i.e., notably lower than quartz, feldspar, and granite (~0.6–0.8; Byerlee, 1966, 1978; Ikari et al., 2011). Structural relationships are similar to the localized deformation along principal slip surfaces developed within weaker minerals within highly competent country rock observed in other brittle faults, such as the Zuccale fault, Italy (Collettini et al., 2009), San Andreas fault, California (Moore and Rymer, 2007), Naukluft thrust, Namibia (Faber et al., 2014), and Wasatch fault, Utah (Evans

et al., 2014; Ault et al., 2015). In polyphase rocks, <10% hematite causes dramatic strain weakening and localization during experiments (Gonçalves et al., 2015). Similarly, in laboratory deformation experiments and numerical models, strain localization along thin slip surfaces is often attributed to kinematic constraints of rigid forcing blocks or strong materials on the weaker deforming material (Mandl et al., 1977; Ikari et al., 2011; Gardner et al., 2017; Rattez and Veveakis, 2020).

Several lines of microstructural and geochemical evidence support high temperatures during fault mirror development. First, the polygonal grain morphology and sintered textures near the fault mirror surface in samples MC14-s2 and MC14-s3 are like morphologies observed in other natural hematite fault mirrors (Figs. 3 and 4; Ault et al., 2015; McDermott et al., 2017; Ault et al., 2019), in hematite dry heating experiments (Vallina et al., 2014), and in high-gloss experimental faults in carbonate gouge (Fondriest et al., 2013; Pozzi et al., 2018). Temperature rises modeled from textures and thermochronometry data patterns along natural and experimental hematite fault mirrors are >1000 °C and >900 °C, respectively (McDermott et al., 2017; Calzolari et al., 2020). Polygonal textures in hematite may reflect grain growth, sintering, and/or recrystallization, which are all temperaturemediated processes (McDermott et al., 2017; Ault et al., 2019; Calzolari et al., 2020). Second, polygonal grains within ~5 µm of the fault mirror surface in these same samples are larger than the largest grain/subgrain in the underlying cataclasite (Figs. 3B and 3K). Our observed grain-size reduction perpendicular to the fault mirror surface is consistent with a fault mirror-perpendicular thermal gradient and resulting grain growth patterns (cf. Ault et al., 2019).

Sample MC14-s2 exhibits a continuous, featureless layer of Fe-oxide at the fault mirror surface above the polygonal grains (Figs. 3B and 3D). Additional transmission electron microscope (TEM) observations are required to confirm if this material is amorphous. If this layer was hydrous, it may represent a solidified, relict Fe-oxide "gel" layer analogous to a silica gel (e.g., Di Toro et al., 2004; Kirkpatrick et al., 2013; Faber et al., 2014; Rowe et al., 2019). Regardless of its origin, trace Si and P in this surface layer, and trace amounts of Si in the underlying polygonal grains (Fig. S3) provide evidence of high temperatures during their formation. Experiments involving heating ferrihydrite to ~800 °C indicated that Si and P are incorporated into neoformed hematite (Gálvez et al., 1999; Campbell et al., 2002; Cornell and Schwertmann, 2003). However, when Si concentrations exceed a critical threshold  $(X_{Si} \ge 0.134)$ , Si is expelled from the hematite and forms a poorly crystalline Si-Fe-O phase (Campbell et al., 2002). It is possible the polygonal grains with trace Si and overlying Si-enriched Fe-oxide layer at the fault mirror surface may have formed concurrently by an analogous, natural high-temperature mechanism, although more work is required to characterize the crystallinity and establish a genetic relationship between these two layers.

## Fault Composition Control of Frictional Heat Generation and Dynamic Weakening

The field, microstructural, and geochemical evidence of strain localization and high temperatures along the fault mirror surface implies that these fault mirrors developed during seismic slip (Rowe and Griffith, 2015). In addition, comminuted hematite in the fault mirror volume (domain 1) and, to a lesser degree, in the underlying cataclasite (domain 2) also support but do not require coseismic slip on these surfaces (Stünitz et al., 2010). We do not know the incremental or total displacement along these faults, making it challenging to constrain the magnitude of individual earthquakes. Based on the surface area of the fault mirrors (approximately square centimeter scale), displacement per event was likely at the micrometer to less than centimeter scale and indicative of small-magnitude events. It is unclear whether this microseismicity nucleated in the uppermost seismogenic zone or represents triggered slip or aftershocks associated with larger events that nucleated at depth. Regardless, data from these small fault mirrors inform the mechanics of small earthquakes and may have implications for larger events if earthquakes are self-similar (e.g., Ide and Beroza, 2001).

We observe clear relationships in the La Luz samples between fault mirror volume grain morphologies and textures reflecting elevated temperatures, the thickness of the deforming zone (which we define as domain 1 plus domain 2), and proportions of hematite to host rock within the deforming zone. Observed microstructures suggest variable coseismic temperature rise between samples, with the most pervasive polygonal grains representing the highest temperatures (Fig. 4). Aliquots with a thinner deforming zone and higher relative abundance of host rock particles have textures indicative of higher temperatures along the fault mirror surface (Figs. 4 and 9). For example, MC14-s2 has the thinnest deforming zone of 48-65 µm (e.g., domain 1 = 8-15  $\mu$ m thick, domain 2 = 40-50  $\mu$ m thick) and highest percentage of host rock guartz and feldspar grains, with 31% and 87% in domain 1 and 2, respectively. Sample MC14-s2 has the most pervasive and thickest layer of polygonal grains (~2.5-5 µm thick), as well as the featureless layer containing Si and P along the slip interface—textures collectively interpreted to represent the highest fault slip temperatures. In sample MC14-s3, the deforming zone is thicker (~65-110 µm thick), and there is a lower relative abundance of host rock grains in both domains, with 7% in domain 1 and 38%-55% in domain 2 (Figs. 4 and 9). This fault mirror surface exhibits polygonal hematite grains, but this layer is thinner (~2-2.5 µm thick) than in sample MC14-s2, implying lower peak temperatures. Sample MC14-s5 has the thickest deforming zone and the lowest proportion of host rock particles (6% and 16% in domains 1 and 2, respectively). The fault mirror surface comprises comminuted, rounded hematite grains and broken hematite plates and lacks polygonal grains, suggesting the lowest peak fault slip temperatures of the La Luz sample suite (Figs. 4 and 9). Although we do not know if domain 1 and domain 2 textures developed concurrently, the patterns and relationships we observed hold whether the deformation that produced fault mirror surface and domain 1 grain morphologies involved both domains 1 and 2, or

Together, these observations illustrate the combined role of the deforming zone thickness and bulk strength of fault materials in contributing

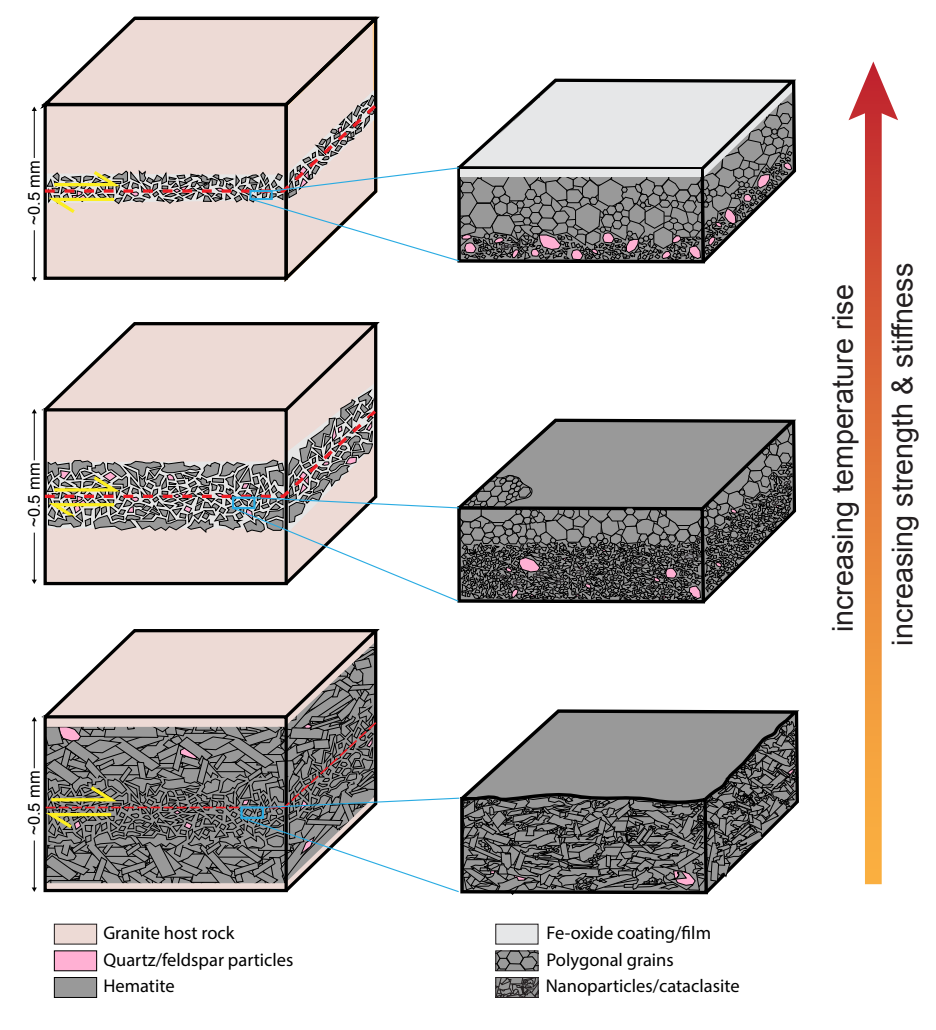


Figure 9. Schematic block diagrams showing the relationships between thickness and composition of the hematite-rich deforming zone (domains 1 and 2) and fault mirror surface textures, with inferred relative fault strength and stability and coseismic temperature rise.

to the magnitude of coseismic temperature rise. Higher-temperature hematite morphologies are associated with thinner deforming zones (Figs. 4 and 9), consistent with temperature rise-fault zone thickness patterns inferred from biomarkers from the Muddy Mountain thrust fault (Coffey et al.,

2019) and empirically predicted and experimentally observed relationships for coseismic frictional heating (Cardwell et al., 1978; Lachenbruch, 1986; Goldsby and Tullis, 2011). The equation for temperature rise along a fault surface is  $T_{\rm surf} = (\mu\sigma_{\rm n}Vt/2\rho Ch) + T_{\rm amb}$ , where  $\mu$  is the coefficient of

friction,  $\sigma_n$  is normal stress, V is slip velocity, t is duration of slip,  $\rho$  is density, C is heat capacity, h is half-width of the deforming zone, and  $T_{amb}$  is ambient temperature (Lachenbruch, 1986). Thus, temperature rise along the fault mirror surface is inversely proportional to the thickness of the deforming zone and proportional to u, although temperature also depends on the length scale over which heat diffuses (Fig. 9). In addition, the maximum strength of the seismogenic crust is generally assumed to be the frictional resistance to sliding on an optimally oriented fault plane, so  $\mu$  is a proxy for fault strength (e.g., Brace and Kohlstedt, 1980; Kohlstedt et al., 1995; Brantut and Platt, 2017). Hematite is weak (Calzolari et al., 2020), but the presence of quartz and feldspar grains may lead to higher bulk  $\mu$  values (Rattez and Veveakis, 2020, and references therein). We suggest that samples with higher proportions of host-rock-derived guartz and feldspar grains in the deforming zone have higher bulk u values, which contribute constructively to a higher magnitude of temperature rise (Figs. 4 and 9).

These same two factors (deforming zone thickness and material properties) also influence the stiffness of the fault and may further promote strain localization during small-moment-magnitude earthquakes. Stiffness is related to the fault surroundings, which is the deformation apparatus itself in the laboratory and the wall rock in nature (Cook, 1981; Rice and Ruina, 1983; Scholz, 1998; Beeler, 2007; Leeman et al., 2015, 2016, 2018; Ikari, 2019). In our studied natural fault mirrors, the proximity between the stronger granite and the fault mirror slip surface that preferentially developed in hematite results in a "stiffer" system (cf. samples MC14-s2 and MC14-s5; Fig. 9). Additionally, higher proportions of quartz and feldspar particles may also increase the effective stiffness (Leeman et al., 2015). Deformation experiments have revealed that stiffer systems promote strain localization, and this strain localization, in turn, can increase a fault's critical stiffness as slip progresses (e.g., Leeman et al., 2016, 2018). We suggest that, in our crystalline basement-hosted hematite fault mirrors, these factors may create a positive feedback that leads to higher coseismic temperature rise associated with

higher effective stiffness in thinner, more quartzand feldspar-rich deforming zones (Fig. 9).

Different peak temperatures along these fault mirror surfaces may have led to different dynamic weakening mechanisms that promoted propagation of small-moment-magnitude earthquakes (e.g., Di Toro et al., 2011, and references therein). For example, fault mirrors that experienced the highest peak temperatures characterized by pervasive polygonal hematite grains may have experienced initial flash heating and/or shear heating, resulting in amorphization at high temperatures and/or melting, followed by grain growth in what is now the fault mirror volume (i.e., samples MC14-s2 and MC14-s3; Rice, 2006; McDermott et al., 2017; Ault et al., 2019; Rowe et al., 2019). Surfaces characterized by cataclastic nanoparticles may have experienced weakening due to nanoparticle lubrication (i.e., samples MC14-s5 and MC13-TC; Han et al., 2007, 2010, 2011; De Paola et al., 2011). If the observed featureless layer along the slip surface of sample MC14-s2 represents a solidified relict gel layer, gel lubrication may have been another mechanism influencing fault strength along some surfaces (e.g., Brodsky and Kanamori, 2001; Di Toro et al., 2006). Additional structural and textural observations from this surface layer, domain 1, and domain 2 are required to pinpoint weakening mechanisms (cf. Pozzi et al., 2019).

## **Rio Grande Rift Exhumation and Seismicity**

Hematite fault mirrors preserve textural evidence of fault reactivation, strain localization, and transient, elevated temperatures during past seismic slip. Hematite He thermochronometry data patterns reveal that some hematite likely formed prior to inception of the Rio Grande rift. Fault slip temperatures  $\geq 800\,^{\circ}$ C at ambient temperatures less than the hematite  $T_c$  would promote He loss via thermally activated volume diffusion and/or hematite regrowth or recrystallization in the fault mirror volume (McDermott et al., 2017; Ault, 2020; Calzolari et al., 2020). If fault slip occurred at ambient temperatures greater than the hematite  $T_c$ , it would not be reflected in the hematite He budget. With this

context, the hematite He dates from aliquots from the fault mirror volume of these surfaces may reflect two possible scenarios. First, seismicity occurred along these faults at depth during a pre–Rio Grande rift tectonic event(s). This deformation created the observed hematite grain-size distributions with  $T_{\rm c}$  sensitive to the ambient thermal conditions, and hematite in domain 1 "passively" recorded Rio Grande rift cooling. Second, seismicity occurred on these hematite fault mirrors coeval with Rio Grande rift fault processes and rift flank exhumation. However, thermochronometry alone cannot discriminate between exhumation-related cooling and He loss associated with frictional heating.

Although it is challenging to discriminate between these hypotheses, we prefer the second scenario of coeval exhumation and seismicity along these faults because it is consistent with the integrated field, microstructural, and thermochronometric data. First, the fault mirror orientations and dip-slip slickenlines (Figs. 2E and 2I) are most consistent with roughly SW-NE and E-W extension and Rio Grande rift-compatible deformation (e.g., Chapin and Cather, 1994). Second, Tijeras fault mirrors are collocated with the trace of the Sandia fault, a Rio Grande rift structure. La Luz samples are collocated with the La Cueva fault, which has an inferred history that predates the Rio Grande rift (Karlstrom et al., 1999a). La Luz hematite was likely reactivated during Rio Grande rift-related fault slip. Third, hematite He dates from sample MC14-s5A are younger than expected from thermal history models (Fig. 8D). This suggests additional He loss associated with friction-generated heat on this fault mirror surface at or below the hematite  $T_c$ . Thus, these data collectively capture Rio Grande rift seismicity concurrent with regional rift flank exhumation. It is permissible and likely that some deformation on the current hematite fault mirrors occurred during the Ancestral Rockies and/or Laramide orogenies, but these small faults were ultimately reactivated during Rio Grande rift-related deformation.

Based on this interpretation, hematite He dates provide constraints on the timing, ambient thermal conditions, and crustal depths of Rio Grande rift seismicity. The hematite He dates between ca. 25 and 10 Ma are consistent with incipient rifting

during the late Oligocene and rapid exhumation of the rift flank from ca. 25 to 10 Ma (e.g., Chapin and Cather, 1994; Ingersoll, 2001; House et al., 2003; Ricketts et al., 2015). In this scenario, the seismicity occurred at ambient temperatures of ≥110-60 °C, which correspond to depths of ≥3.1-1.7 km, assuming a geothermal gradient of 35 °C/km as determined for conditions during rifting by House et al. (2003), or ~3.8-2 km for the modern-day geothermal gradient of 29 °C/km (Fig. 10). If hematite He loss associated with seismicity occurred at temperatures at or greater than the hematite He  $T_{c}$ , then the depth of these events is ≥3.1 km. There are no hematite He dates from fault mirror volume aliquots younger than hostrock apatite He dates (Fig. 7), suggesting that there was no coseismic He loss at ambient temperatures <60 °C or <2 km. The depth of seismogenesis along these hematite fault mirrors (~2-4 km) is similar to nanoearthquakes to microearthquakes

documented along minor hematite fault mirrors in the Wasatch fault damage zone (~2–3 km; Ault et al., 2015; McDermott et al., 2017; see also Fig. 10 here). We thus suggest that hematite fault mirrors can capture coseismic processes operating at similar depths in the uppermost seismogenic zone of normal fault systems.

## CONCLUSIONS

Field observations, microstructural analysis, and (U-Th)/He thermochronometry from hematite fault mirrors in the eastern rift flank of the Rio Grande rift in the Sandia Mountains, New Mexico, provide important insights from naturally deformed fault rocks into the in situ conditions and properties associated with seismicity at crustal depths of ~2–4 km. Fault and slickenline orientations, comparison of hematite He dates from fault mirror volumes

Sandia Mountains

La Luz samples

Albuquerque, NM

Sandia Mountains

La Luz samples

La Luz samples

Apatite He

Masatch FM seismicity

hematite Fle

Sandia FM seismicity

Sandia FM seismicity

seismic tremor & slow slip
aseismic treep

Figure 10. Schematic crustal section of the Sandia Mountains near Albuquerque representing the depths of the earthquakes recorded by hematite fault mirrors (FMs), with Wasatch estimates of McDermott et al. (2017) for comparison. Blue, purple, and green boxes represent the closure temperature ( $T_c$ ) of zircon (U-Th)/He (He), apatite He, and hematite He, respectively, with associated crustal depths assuming a geothermal gradient of 35 °C/km.

with other low-temperature thermochronometers (apatite He, AFT, and zircon He), and thermal history modeling suggest hematite He dates record small-moment-magnitude events associated with Rio Grande rift extension ca. 25 to 10 Ma.

Hematite microstructures provide evidence of fault reactivation, intense strain localization, and high temperatures (likely ≥800 °C) at the fault mirror surface. The prevalence and distribution of these textures correspond to the thickness and mineral composition of the deforming zone. Fault mirrors characterized by thinner, hematite-rich deforming zones with higher proportions of host-rock quartz and feldspar result in higher effective fault strength and stiffness, and a higher proportion of hightemperature hematite grain morphologies. Thicker deforming zones with lower proportions of hostrock material have lower strength and stiffness and likely experienced lower peak temperatures. Our observations are consistent with empirical relationships and laboratory deformation experiments investigating factors governing fault stability and frictional heating. Thus, these hematite fault mirrors provide a natural example of the ways in which fault zone thickness and composition control the fault strength, magnitude of coseismic temperature rise, and potentially the dynamic weakening mechanisms operative on thin slip surfaces.

#### ACKNOWLEDGMENTS

We thank FenAnn Shen, Pete Reiners, and Uttam Chowdhury for analytical assistance, and Tomas Capaldi and Dennis Newell for insightful discussions. We also thank Randy Williams and Catherin Mottram for insightful and thorough reviews that helped to improve this paper, and Andrea Hampel for editorial handling. This work was supported by a National Science Foundation (NSF) Postdoctoral Fellowship grant (EAR-1952905) to Odlum and NSF CAREER grant (EAR-1654628) to Ault.

#### REFERENCES CITED

Abbott, J.C., and Goodwin, L.B., 1995, A spectacular exposure of the Tijeras fault, with evidence for Quaternary motion, in Bauer, P.W., Kues, B.S., Dunbar, N.W., Karlstrom, K.E., and Harrison, B., eds., Geology of the Santa Fe Region, New Mexico: New Mexico Geological Society Guidebook 46, p. 117–125.

Abbott, J.C., Goodwin, L.B., Kelley, S.A., Maynard, S.R., and McIntosh, W.C., 2004, The anatomy of a long-lived fault system: Structural and thermochronologic evidence for

- Laramide to Quaternary activity in the Tijeras fault system, New Mexico, *in* Cather, S.M., McIntosh, W.C., and Kelley, S.A., eds., Tectonics, Geochronology, and Volcanism in the Southern Rocky Mountains and Rio Grande Rift: New Mexico Bureau of Geology and Mineral Resources Bulletin 160, p. 113–138, https://geoinfo.nmt.edu/publications/monographs/bulletins/downloads/160/papers/06abbot.pdf.
- Abràmoff, M.D., Magalhães, P.J., and Ram, S.J., 2004, Image processing with ImageJ: Biophotonics International, v. 11, p. 36–42.
- Aldrich, M.J., Chapin, C.E., and Laughlin, A.W., 1986, Stress history and tectonic development of the Rio Grande rift, New Mexico: Journal of Geophysical Research–Solid Earth, v. 91, p. 6199–6211, https://doi.org/10.1029/JB091iB06p06199.
- Allmendinger, R.W., Cardozo, N.C., and Fisher, D., 2013, Structural Geology Algorithms: Vectors & Tensors: Cambridge, UK, Cambridge University Press, 289 p.
- Ault, A.K., 2020, Hematite fault rock thermochronometry and textures inform fault zone processes: Journal of Structural Geology, v. 133, p. 104002, https://doi.org/10.1016/j.jsg.2020 .104002.
- Ault, A.K., Reiners, P.W., Evans, J.P., and Thomson, S.N., 2015, Linking hematite (U-Th)/He dating with the microtextural record of seismicity in the Wasatch fault damage zone, Utah, USA: Geology, v. 43, no. 9, p. 771–774, https://doi.org/10 .1130/G36897.1.
- Ault, A.K., Guenthner, W.R., Moser, A.C., Miller, G.H., and Refsnider, K.A., 2018, Zircon grain selection reveals (de)coupled metamictization, radiation damage, and He diffusivity: Chemical Geology, v. 490, p. 1–12, https://doi.org/10.1016 /i.chemgeo.2018.04.023.
- Ault, A.K., Jensen, J.L., McDermott, R.G., Shen, F.A., and Van Devener, B.R., 2019, Nanoscale evidence for temperature-induced transient rheology and postseismic fault healing: Geology, v. 47, no. 12, p. 1203–1207, https://doi.org/10.1130 //G46317.1.
- Balout, H., Roques, J., Gautheron, C., Tassan-Got, L., and Mbongo-Djimbi, D., 2017, Helium diffusion in pure hematite (α-Fe<sub>2</sub>O<sub>3</sub>) for thermochronometric applications: A theoretical multi-scale study: Computational & Theoretical Chemistry, v. 1099, p. 21–28, https://doi.org/10.1016/j.comptc.2016.11.001.
- Beeler, N.M., 2007, Laboratory-observed faulting in intrinsically and apparently weak materials: Strength, seismic coupling, dilatancy, and pore fluid pressure, in Dixon, T.H., and Moore, J.C., eds., The Seismogenic Zone of Subduction Thrust Faults: New York, Columbia University Press, p. 370–449, https://doi.org/10.7312/dixo13866-013.
- Beeler, N.M., Tullis, T.E., and Goldsby, D.L., 2008, Constitutive relationships and physical basis of fault strength due to flash heating: Journal of Geophysical Research–Solid Earth, v. 113, B01401, https://doi.org/10.1029/2007JB004988.
- Berglund, H.T., Sheehan, A.F., Murray, M.H., Roy, M., Lowry, A.R., Nerem, R.S., and Blume, F., 2012, Distributed deformation across the Rio Grande rift, Great Plains, and Colorado Plateau: Geology, v. 40, no. 1, p. 23–26, https://doi.org/10.1130/G32418.1.
- Borhara, K., and Onasch, C.M., 2020, Evidence for silica gel and its role in faulting in the Tuscarora Sandstone: Journal of Structural Geology, v. 139, p. 104140, https://doi.org/10.1016/j.jsq.2020.104140.
- Brace, W.F., and Kohlstedt, D.L., 1980, Limits on lithospheric stress imposed by laboratory experiments: Journal of

ere/article-pdf/18/1/241/5515844/241.pdf

- Geophysical Research–Solid Earth, v. 85, no. B11, p. 6248–6252, https://doi.org/10.1029/JB085iB11p06248.
- Brantut, N., and Platt, J.D., 2017, Dynamic weakening and the depth dependence of earthquake faulting, *in* Thomas, M.Y., Mitchell, T.M., and Bhat, H.S., eds., Fault Zone Dynamic Processes: Evolution of Fault Properties during Seismic Rupture: American Geophysical Union Geophysical Monograph 227, p. 171–194, https://doi.org/10.1002/9781119156895.ch9.
- Brodsky, E.E., and Kanamori, H., 2001, Elastohydrodynamic lubrication of faults: Journal of Geophysical Research–Solid Earth, v. 106, no. B8, p. 16357–16374, https://doi.org/10.1029/2001JB000430.
- Byerlee, J., 1978, Friction of rocks, in Byerlee, J.D., and Wyss, M., eds., Rock Friction and Earthquake Prediction: Basel, Switzerland, Birkhäuser, Contributions to Current Research in Geophysics (CCRG) 6, p. 615–626, https://doi.org/10.1007 /978-3-0348-7182-2\_4.
- Byerlee, J.D., 1966, The Frictional Characteristics of Westerly Granite [Ph.D. dissertation]: Cambridge, Massachusetts, Massachusetts Institute of Technology, 179 p., https://dspace.mit.edu/handle/1721.1/52952.
- Calzolari, G., Ault, A.K., Hirth, G., and McDermott, R.G., 2020, Hematite (U-Th)/He thermochronometry detects asperity flash heating during laboratory earthquakes: Geology, v. 48, no. 5, p. 514–518, https://doi.org/10.1130/G46965.1.
- Campbell, A.S., Schwertmann, U., Stanjek, H., Friedl, J., Kyek, A., and Campbell, P.A., 2002, Si incorporation into hematite by heating Si-ferrihydrite: Langmuir, v. 18, no. 21, p. 7804–7809, https://doi.org/10.1021/la011741w.
- Cardozo, N., and Allmendinger, R.W., 2013, Spherical projections with OSXStereonet: Computers & Geosciences, v. 51, p. 193–205, https://doi.org/10.1016/j.cageo.2012.07.021.
- Cardwell, R.K., Chinn, D.S., Moore, G.F., and Turcotte, D.L., 1978, Frictional heating on a fault zone with finite thickness: Geophysical Journal International, v. 52, no. 3, p. 525–530, https://doi.org/10.1111/j.1365-246X.1978.tb04247.x.
- Cather, S.M., Chamberlin, R.M., Chapin, C.E., and McIntosh, W.C., 1994, Stratigraphic consequences of episodic extension in the Lemitar Mountains, central Rio Grande Rift, *in* Keller, G.R., and Cather, S.M., eds., Basins of the Rio Grande Rift: Structure, Stratigraphy and Tectonic Setting: Geological Society of America Special Paper 291, p. 157–170, https://doi.org/10.1130/SPE291-p157.
- Cather, S.M., Mack, G.H., and Giles, K.A., 2004, Laramide orogeny in central and northern New Mexico and southern Colorado, in Mack, G.H., and Giles, K.A., eds., The Geology of New Mexico, A Geologic History: New Mexico Geological Society Special Publication 11, p. 203–248.
- Catling, D.C., and Moore, J.M., 2003, The nature of coarsegrained crystalline hematite and its implications for the early environment of Mars: Icarus, v. 165, no. 2, p. 277–300, https://doi.org/10.1016/S0019-1035(03)
- Chapin, C.E., and Cather, S.M., 1994, Tectonic settings of the axial basins of the northern and central Rio Grande rift, in Keller, G.R., and Cather, S.M., eds., Basins of the Rio Grande Rift: Structure, Stratigraphy and Tectonic Setting: Geological Society of America Special Paper 291, p. 5–26, https://doi.org/10.1130/SPE291-p5.
- Chapin, C.E., Wilks, M., McIntosh, W.C., and Cather, S.M., 2004, Space-time patterns of Late Cretaceous to present magmatism: New Mexico—Comparison with Andean volcanism

- and potential for future volcanism, *in* Cather, S.M., McIntosh, W.C., and Kelley, S.A., eds., Tectonics, Geochronology, and Volcanism in the Southern Rocky Mountains and Rio Grande Rift: New Mexico Bureau of Geology and Mineral Resources Bulletin 160, p. 13–40, https://geoinfo.nmt.edu/publications/monographs/bulletins/downloads/160/papers/02chapin.pdf.
- Coffey, G.L., Savage, H.M., Polissar, P.J., Rowe, C.D., and Rabinowitz, H.S., 2019, Hot on the trail: Coseismic heating on a localized structure along the Muddy Mountain fault, Nevada: Journal of Structural Geology, v. 120, p. 67–79, https://doi.org/10.1016/j.jsg.2018.12.012.
- Collettini, C., Niemeijer, A., Viti, C., and Marone, C., 2009, Fault zone fabric and fault weakness: Nature, v. 462, no. 7275, p. 907–910, https://doi.org/10.1038/nature08585.
- Collettini, C., Viti, C., Tesei, T., and Mollo, S., 2013, Thermal decomposition along natural carbonate faults during earthquakes: Geology, v. 41, no. 8, p. 927–930, https://doi.org /10.1130/G34421.1.
- Cook, N.G., 1981, Stiff testing machines, stick slip sliding, and the stability of rock deformation, in Carter, N.L., Friedman, M., Logan, J.M., and Stearns, D.W., eds., Mechanical Behavior of Crustal Rocks: The Handin Volume: American Geophysical Union Geophysical Monograph 24, p. 93–102, https:// doi.org/10.1029/GM024p0093.
- Cornell, R.M., and Schwertmann, U., 2003, The Iron Oxides: Structure, Properties, Reactions, Occurrences and Uses: New York, John Wiley & Sons, 121 p., https://doi.org/10 .1002/3527602097.
- De Paola, N., Hirose, T., Mitchell, T., Di Toro, G., Viti, C., and Shimamoto, T., 2011, Fault lubrication and earthquake propagation in thermally unstable rocks: Geology, v. 39, no. 1, p. 35–38, https://doi.org/10.1130/G31398.1.
- Di Toro, G., Goldsby, D.L., and Tullis, T.E., 2004, Friction falls towards zero in quartz rock as slip velocity approaches seismic rates: Nature, v. 427, no. 6973, p. 436–439, https://doi .org/10.1038/nature02249.
- Di Toro, G., Hirose, T., Nielsen, S., Pennacchioni, G., and Shimamoto, T., 2006, Natural and experimental evidence of melt lubrication of faults during earthquakes: Science, v. 311, no. 5761, p. 647–649, https://doi.org/10.1126/science .1121012.
- Di Toro, G., Han, R., Hirose, T., De Paola, N., Nielsen, S., Mizo-guchi, K., Ferri, F., Cocco, M., and Shimamoto, T., 2011, Fault lubrication during earthquakes: Nature, v. 471, no. 7339, p. 494–498, https://doi.org/10.1038/nature09838.
- Dickinson, W.R., and Snyder, W.S., 1978, Plate tectonics of the Laramide orogeny, in Matthews, V., III, ed., Laramide Folding Associated with Basement Block Faulting in the Western United States: Geological Society of America Memoir 151, p. 355–366, https://doi.org/10.1130/MEM151-p355.
- Dideriksen, K., Christiansen, B.C., Baker, J.A., Frandsen, C., Balic-Zunic, T., Tullborg, E., Mørup, S., and Stipp, S.L.S., 2007, Fe-oxide fracture fillings as a palaeo-redox indicator: Structure, crystal form and Fe isotope composition: Chemical Geology, v. 244, no. 1–2, p. 330–343, https://doi.org/10.1016/j.chemgeo.2007.06.027.
- Dieterich, J.H., 1986, A model for the nucleation of earthquake slip, in Das, S., Boatwright, J., and Scholz, C.H., eds., Earthquake Source Mechanics: American Geophysical Union Geophysical Monograph 37, p. 37–47, https://doi.org/10 .1029/GM037p0037.

- Dodson, M.H., 1973, Closure temperature in cooling geochronological and petrological systems: Contributions to Mineralogy and Petrology, v. 40, no. 3, p. 259–274, https://doi.org/10.1007/BF00373790.
- Evans, J.P., Prante, M.R., Janecke, S.U., Ault, A.K., and Newell, D.L., 2014, Hot faults: Iridescent slip surfaces with metallic luster document high-temperature ancient seismicity in the Wasatch fault zone, Utah, USA: Geology, v. 42, no. 7, p. 623–626, https://doi.org/10.1130/G35617.1.
- Evenson, N.S., Reiners, P.W., Spencer, J.E., and Shuster, D.L., 2014, Hematite and Mn oxide (U-Th)/He dates from the Buckskin-Rawhide detachment system, western Arizona: Gaining insights into hematite (U-Th)/He systematics: American Journal of Science, v. 314, no. 10, p. 1373–1435, https://doi.org/10.2475/10.2014.01.
- Faber, C., Rowe, C.D., Miller, J.A., Fagereng, Å., and Neethling, J.H., 2014, Silica gel in a fault slip surface: Field evidence for palaeo-earthquakes?: Journal of Structural Geology, v. 69, p. 108–121, https://doi.org/10.1016/j.jsg.2014.09.021.
- Farley, K.A., 2018, Helium diffusion parameters of hematite from a single-diffusion-domain crystal: Geochimica et Cosmochimica Acta, v. 231, p. 117–129, https://doi.org/10.1016/j .qca.2018.04.005.
- Farley, K.A., and Flowers, R.M., 2012, (U-Th)/Ne and multi-domain (U-Th)/He systematics of a hydrothermal hematite from eastern Grand Canyon: Earth and Planetary Science Letters, v. 359, p. 131–140, https://doi.org/10.1016/j.epsl.2012.10.010.
- Farley, K.A., and McKeon, R., 2015, Radiometric dating and temperature history of banded iron formation-associated hematite, Gogebic iron range, Michigan, USA: Geology, v. 43, no. 12, p. 1083–1086, https://doi.org/10.1130/G37190.1.
- Farley, K.A., Wolf, R.A. and Silver, L.T., 1996, The effects of long alpha-stopping distances on (U-Th)/He ages: Geochimica et Cosmochimica Acta, v. 60, p. 4223–4229.
- Ferreira, F., Lagoeiro, L., Morales, L.F., de Oliveira, C.G., Barbosa, P., Ávila, C., and Cavalcante, G.C., 2016, Texture development during progressive deformation of hematite aggregates: Constraints from VPSC models and naturally deformed iron oxides from Minas Gerais, Brazil: Journal of Structural Geology, v. 90, p. 111–127, https://doi.org/10.1016/j.jsg.2016.07.009.
- Flowers, R.M., and Kelley, S.A., 2011, Interpreting data dispersion and "inverted" dates in apatite (U-Th)/He and fission-track datasets: An example from the US midcontinent: Geochimica et Cosmochimica Acta, v. 75, p. 5169–5186, https://doi.org/10.1016/j.gca.2011.06.016.
- Flowers, R.M., Ketcham, R.A., Shuster, D.L., and Farley, K.A., 2009, Apatite (U-Th)/He thermochronometry using a radiation damage accumulation and annealing model: Geochimica et Cosmochimica Acta, v. 73, no. 8, p. 2347–2365, https://doi.org/10.1016/j.gca.2009.01.015.
- Flowers, R.M., Farley, K.A., and Ketcham, R.A., 2015, A reporting protocol for thermochronologic modeling illustrated with data from the Grand Canyon: Earth and Planetary Science Letters, v. 432, p. 425–435, https://doi.org/10.1016/j.epsl.2015.09.053.
- Fondriest, M., Smith, S.A., Candela, T., Nielsen, S.B., Mair, K., and Di Toro, G., 2013, Mirror-like faults and power dissipation during earthquakes: Geology, v. 41, no. 11, p. 1175–1178, https://doi.org/10.1130/G34641.1.

ere/article-pdf/18/1/241/5515844/241.pdf

- Gallagher, K., Brown, R., and Johnson, C., 1998, Fission track analysis and its applications to geological problems: Annual Review of Earth and Planetary Sciences, v. 26, no. 1, p. 519– 572, https://doi.org/10.1146/annurev.earth.26.1.519.
- Gálvez, N., Barron, V., and Torrent, J., 1999, Preparation and properties of hematite with structural phosphorus: Clays and Clay Minerals, v. 47, no. 3, p. 375–385, https://doi.org /10.1346/CCMN.1999.0470314.
- Gardner, R., Piazolo, S., Evans, L., and Daczko, N., 2017, Patterns of strain localization in heterogeneous, polycrystalline rocks—A numerical perspective: Earth and Planetary Science Letters, v. 463, p. 253–265, https://doi.org/10.1016/j.epsl.2017.01.039.
- Geissman, J.W., and Harlan, S.S., 2002, Late Paleozoic remagnetization of Precambrian crystalline rocks along the Precambrian/Carboniferous nonconformity, Rocky Mountains: A relationship among deformation, remagnetization, and fluid migration: Earth and Planetary Science Letters, v. 203, no. 3–4, p. 905–924, https://doi.org/10.1016/S0012-921X(02)00932-9.
- Goldsby, D.L., and Tullis, T.E., 2011, Flash heating leads to low frictional strength of crustal rocks at earthquake slip rates: Science, v. 334, no. 6053, p. 216–218, https://doi.org/10.1126/ science.1207902.
- Gonçalves, C.C., Gonçalves, L., and Hirth, G., 2015, The effects of quartz recrystallization and reaction on weak phase interconnection, strain localization and evolution of microstructure: Journal of Structural Geology, v. 71, p. 24–40, https://doi.org/10.1016/j.jsg.2014.11.010.
- Guenthner, W.R., Reiners, P.W., Ketcham, R.A., Nasdala, L., and Giester, G., 2013, Helium diffusion in natural zircon: Radiation damage, anisotropy, and the interpretation of zircon (U-Th)/He thermochronology: American Journal of Science, v. 313, no. 3, p. 145–198, https://doi.org/10.2475/03.2013.01.
- Han, R., Shimamoto, T., Ando, J.I., and Ree, J.H., 2007, Seismic slip record in carbonate-bearing fault zones: An insight from high-velocity friction experiments on siderite gouge: Geology, v. 35, no. 12, p. 1131–1134, https://doi.org/10.1130 /G24106A.1.
- Han, R., Hirose, T., and Shimamoto, T., 2010, Strong velocity weakening and powder lubrication of simulated carbonate faults at seismic slip rates: Journal of Geophysical Research–Solid Earth, v. 115, B03412, https://doi.org/10.1029 /2008JB006136.
- Han, R., Hirose, T., Shimamoto, T., Lee, Y., and Ando, J.I., 2011, Granular nanoparticles lubricate faults during seismic slip: Geology, v. 39, no. 6, p. 599–602, https://doi.org/10.1130/G31842.1.
- Hirono, T., Kaneki, S., Ishikawa, T., Kameda, J., Tonoike, N., Ito, A., and Miyazaki, Y., 2020, Generation of sintered fault rock and its implications for earthquake energetics and fault healing: Communications Earth & Environment, v. 1, no. 1, p. 1–8, https://doi.org/10.1038/s43247-020-0004-z.
- Holland, M.E., Grambling, T.A., Karlstrom, K.E., Jones, J.V., Ill, Nagotko, K.N., and Daniel, C.G., 2020, Geochronologic and Hf-isotope framework of Proterozoic rocks from central New Mexico, USA: Formation of the Mazatzal crustal province in an extended continental margin arc: Precambrian Research, v. 347, 105820, https://doi.org/10.1016/j.precamres .2020.105820.

- House, M.A., Kelley, S.A., and Roy, M., 2003, Refining the foot-wall cooling history of a rift flank uplift, Rio Grande rift, New Mexico: Tectonics, v. 22, 1060, https://doi.org/10.1029/2002TC001418.
- Houser, L.M., Ault, A.K., Newell, D.L., Evans, J.P., Shen, F.A. and Van Devener, B.R., 2021, Nanoscale textural and chemical evolution of silica fault mirrors in the Wasatch fault damage zone, Utah, USA: Geochemistry, Geophysics, Geosystems, v. 22, e2020GC009368, https://doi.org/10.1029 /2020GC009368.
- Ide, S., and Beroza, G.C., 2001, Does apparent stress vary with earthquake size?: Geophysical Research Letters, v. 28, no. 17, p. 3349–3352, https://doi.org/10.1029/2001GL013106.
- Ikari, M.J., 2019, Laboratory slow slip events in natural geological materials: Geophysical Journal International, v. 218, no. 1, p. 354–387, https://doi.org/10.1093/gji/ggz143.
- Ikari, M.J., Marone, C., and Saffer, D.M., 2011, On the relation between fault strength and frictional stability: Geology, v. 39, no. 1, p. 83–86, https://doi.org/10.1130/G31416.1.
- Ingersoll, R.V., 2001, Structural and stratigraphic evolution of the Rio Grande rift, northern New Mexico and southern Colorado: International Geology Review, v. 43, no. 10, p. 867–891, https://doi.org/10.1080/00206810109465053.
- Jensen, J.L., Siddoway, C.S., Reiners, P.W., Ault, A.K., Thomson, S.N., and Steele-MacInnis, M., 2018, Single-crystal hematite (U-Th)/He dates and fluid inclusions document widespread Cryogenian sand injection in crystalline basement: Earth and Planetary Science Letters, v. 500, p. 145–155, https:// doi.org/10.1016/j.epsl.2018.08.021.
- Karlstrom, K.E., Cather, S.M., Kelley, S.A., Heizler, M.T., Pazzaglia, F.J., and Roy, M., 1999a, Sandia Mountains and Rio Grande rift: Ancestry of structures and history of deformation, in Pazzaglia, F.J., Lucas, S.G., and Austin, G.S., eds., Albuquerque Country: Socorro, New Mexico, New Mexico Geological Society Guidebook, 50th Field Conference, p. 155–165.
- Karlstrom, K.E., Harlan, S.S., Williams, M.L., McLelland, J., Geissman, J.W., and Ahall, K.I., 1999b, Refining Rodinia: Geologic evidence for the Australia-western US connection in the Proterozoic: GSA Today, v. 9, no. 10, p. 1–7, https://doi. org/10.1130/GSAT-1999-10-01-science.
- Karlstrom, K.E., Amato, J.M., Williams, M.L., Heizler, M., Shaw, C.A., Read, A.S., Bauer, P., Mack, G.H., and Giles, K.A., 2004, Proterozoic tectonic evolution of the New Mexico region: A synthesis, in Mack, G.H., and Giles, K.A., eds., The Geology of New Mexico: A Geologic History: New Mexico Geological Society Special Publication, v. 11, p. 1–34.
- Keller, G.R., and Baldridge, W.S., 1999, The Rio Grande rift: A geological and geophysical overview: Rocky Mountain Geology, v. 34, p. 121–130, https://doi.org/10.2113/34.1.121.
- Kelley, S.A., Chapin, C.E., and Corrigan, J., 1992, Late Mesozoic to Cenozoic cooling histories of the flanks of the northern and central Rio Grande rift, Colorado and New Mexico: New Mexico Bureau of Mines and Mineral Resources Bulletin 145, 39 p., https://geoinfo.nmt.edu/publications/monographs/bulletins/downloads/145/B145.pdf.
- Kelley, V.C., 1977, Geology of Albuquerque Basin, New Mexico: New Mexico Bureau of Mines and Mineral Resources Memoir 33, 60 p., https://geoinfo.nmt.edu/publications/monographs/memoirs/downloads/33/Memoir-33.pdf.
- Kelley, V.C., and Northrop, S.A., 1975, Geology of Sandia Mountains and Vicinity, New Mexico: New Mexico Bureau of Mines

- & Mineral Resources Memoir 29, 136 p., https://geoinfo.nmt.edu/publications/monographs/memoirs/downloads/29/Memoir-29.pdf.
- Ketcham, R.A., 2005, Forward and inverse modeling of low-temperature thermochronometry data: Reviews in Mineralogy and Geochemistry, v. 58, no. 1, p. 275–314, https://doi.org /10.2138/rmg.2005.58.11.
- Ketcham, R.A., Carter, A., Donelick, R.A., Barbarand, J., and Hurford, A.J., 2007, Improved modeling of fission-track annealing in apatite: The American Mineralogist, v. 92, no. 5–6, p. 799–810, https://doi.org/10.2138/am.2007.2281.
- Kirby, E., Karlstrom, K.E., Andronicos, C.L., and Dallmeyer, R.D., 1995, Tectonic setting of the Sandia pluton: An orogenic 1.4 Ga granite in New Mexico: Tectonics, v. 14, no. 1, p. 185– 201, https://doi.org/10.1029/94TC02699.
- Kirkpatrick, J.D., Rowe, C.D., White, J.C., and Brodsky, E.E., 2013, Silica gel formation during fault slip: Evidence from the rock record: Geology, v. 41, no. 9, p. 1015–1018, https://doi. org/10.1130/G34483.1.
- Kohlstedt, D.L., Evans, B., and Mackwell, S.J., 1995, Strength of the lithosphere: Constraints imposed by laboratory experiments: Journal of Geophysical Research-Solid Earth, v. 100, no. B9, p. 17587–17602, https://doi.org /10.1029/95J801460.
- Krainer, K., and Lucas, S.G., 2013, The Pennsylvanian Sandia Formation in northern and central New Mexico, in Lucas, S.G., Nelson, W.J., DiMichele, W.A., Spielmann, J.A., Krainer, K., Barrick, J.E., Elrick, S., and Voigt, S., eds., The Carboniferous-Permian Transition in Central New Mexico: New Mexico Museum of Natural History and Science Bulletin 59, p. 77–100, http://carboniferous.stratigraphy.org/files/20130617155827644.pdf.
- Kuo, L.W., Song, S.R., Suppe, J., and Yeh, E.C., 2016, Fault mirrors in seismically active fault zones: A fossil of small earthquakes at shallow depths: Geophysical Research Letters, v. 43, no. 5, p. 1950–1959, https://doi.org/10.1002/2015GL066882.
- Lachenbruch, A.H., 1986, Simple Models for the Estimation and Measurement of Frictional Heating by an Earthquake: U.S. Geological Survey Open-File Report 86-508, 13 p., https://doi.org/10.3133/ofr86508.
- Landman, R.L., and Flowers, R.M., 2013, (U-Th)/He thermochronologic constraints on the evolution of the northern Rio Grande Rift, Gore Range, Colorado, and implications for rift propagation models: Geosphere, v. 9, no. 1, p. 170–187, https://doi.org/10.1130/GES00826.1.
- Leary, R.J., Umhoefer, P., Smith, M.E., Smith, T.M., Saylor, J.E., Riggs, N., Burr, G., Lodes, E., Foley, D., Licht, A., and Mueller, M.A., 2020, Provenance of Pennsylvanian-Permian sedimentary rocks associated with the Ancestral Rocky Mountains orogeny in southwestern Laurentia: Implications for continental-scale Laurentian sediment transport systems: Lithosphere, v. 12, no. 1, p. 88–121, https://doi.org /10.1130/L1115.1.
- Leeman, J., Scuderi, M.M., Marone, C., and Saffer, D., 2015, Stiffness evolution of granular layers and the origin of repetitive, slow, stick-slip frictional sliding: Granular Matter, v. 17, no. 4, p. 447–457, https://doi.org/10.1007/s10035-015-0565-1.
- Leeman, J.R., Saffer, D.M., Scuderi, M.M., and Marone, C., 2016, Laboratory observations of slow earthquakes and the spectrum of tectonic fault slip modes: Nature Communications, v. 7, no. 1, p. 1–6, https://doi.org/10.1038/ncomms11104.

ere/article-pdf/18/1/241/5515844/241.pdf

- Leeman, J.R., Marone, C., and Saffer, D.M., 2018, Frictional mechanics of slow earthquakes: Journal of Geophysical Research–Solid Earth, v. 123, no. 9, p. 7931–7949, https:// doi.org/10.1029/2018JB015768.
- Lewis, C.J., and Baldridge, W.S., 1994, Crustal extension in the Rio Grande rift, New Mexico: Half-grabens, accommodation zones, and shoulder uplifts in the Ladron Peak–Sierra Lucero area, in Keller, G.R., and Cather, S.M., eds., Basins of the Rio Grande Rift: Structure, Stratigraphy, and Tectonic Setting: Geological Society of America Special Paper 291, p. 135–155, https://doi.org/10.1130/SPE291-p135.
- Lipman, P.W., and Mehnert, H.H., 1975, Late Cenozoic basaltic volcanism and development of the Rio Grande depression in the Southern Rocky Mountains, in Curtis, B.F., ed., Cenozoic History of the Southern Rocky Mountains: Geological Society of America Memoir 144, p. 119–154, https://doi.org /10.1130/MEM144-p119.
- Machette, M.N., 1998, Contrasts between short-term and longterm records of seismicity in the Rio Grande rift—Important implications for seismic-hazard assessments in areas of slow extension, *in* Lund, W.R., ed., Western States Seismic Policy Council Proceedings: Utah Geological Survey Miscellaneous Publication 98-2, p. 84–95.
- Mallory, W.W., 1958, Pennsylvanian coarse arkosic redbeds and associated mountains in Colorado: Symposium of Pennsylvanian Rocks of Colorado and Adjacent Areas: Denver, Colorado, Rocky Mountain Association of Geologists, p. 17–21, https://archives.datapages.com/data/rmag /PennRocks58/mallory.htm.
- Mandl, G., De Jong, L.N.J., and Maltha, A., 1977, Shear zones in granular material: Rock Mechanics, v. 9, no. 2–3, p. 95–144, https://doi.org/10.1007/BF01237876.
- McDermott, R.G., Ault, A.K., Evans, J.P., and Reiners, P.W., 2017, Thermochronometric and textural evidence for seismicity via asperity flash heating on exhumed hematite fault mirrors, Wasatch fault zone, UT, USA: Earth and Planetary Science Letters, v. 471, p. 85–93, https://doi.org/10.1016/j.epsl.2017.04.020.
- Mendes, M., and Lagoeiro, L., 2012, Microstructures, crystallographic fabric development and deformation mechanisms in natural hematite aggregates deformed under varied metamorphic conditions: Journal of Structural Geology, v. 40, p. 29–43, https://doi.org/10.1016/j.jsg.2012.04.005.
- Miggins, D.P., Thompson, R.A., Pillmore, C.L., Snee, L.W., and Stern, C.R., 2002, Extension and uplift of the northern Rio Grande rift: Evidence from <sup>40</sup>Ar/<sup>29</sup>Ar geochronology from the Sangre de Cristo Mountains, south-central Colorado and northern New Mexico, in Menzies, M.A., Klemperer, S.L., Ebinger, C.J., and Baker, J., eds., Volcanic Rifted Margins: Geological Society of America Special Paper 362, p. 47–64, https://doi.org/10.1130/0-8137-2362-0-47.
- Moore, D.E., and Rymer, M.J., 2007, Talc-bearing serpentinite and the creeping section of the San Andreas fault: Nature, v. 448, no. 7155, p. 795–797, https://doi.org/10.1038/nature06064.
- Moser, A.C., Evans, J.P., Ault, A.K., Janecke, S.U., and Bradbury, K.K., 2017, (U-Th)/He thermochronometry reveals Pleistocene punctuated deformation and synkinematic hematite mineralization in the Mecca Hills, southernmost San Andreas fault zone: Earth and Planetary Science Letters, v. 476, p. 87–99, https://doi.org/10.1016/j.epsl.2017.07.039.
- Mosher, S., 1998, Tectonic evolution of the southern Laurentian Grenville orogenic belt: Geological Society of America

- Bulletin, v. 110, no. 11, p. 1357–1375, https://doi.org/10.1130/0016-7606(1998)110<1357:TEOTSL>2.3.CO;2.
- Power, W.L., and Tullis, T.E., 1989, The relationship between slickenside surfaces in fine-grained quartz and the seismic cycle: Journal of Structural Geology, v. 11, no. 7, p. 879–893, https://doi.org/10.1016/0191-8141(89)90105-3.
- Pozzi, G., De Paola, N., Nielsen, S.B., Holdsworth, R.E., and Bowen, L., 2018, A new interpretation for the nature and significance of mirror-like surfaces in experimental carbonate-hosted seismic faults: Geology, v. 46, no. 7, p. 583–586, https://doi.org/10.1130/G40197.1.
- Pozzi, G., De Paola, N., Holdsworth, R.E., Bowen, L., Nielsen, S.B., and Dempsey, E.D., 2019, Coseismic ultramylonites: An investigation of nanoscale viscous flow and fault weakening during seismic slip: Earth and Planetary Science Letters, v. 516, p. 164–175, https://doi.org/10.1016/j.epsl.2019.03.042.
- Rattez, H., and Veveakis, M., 2020, Weak phases production and heat generation control fault friction during seismic slip: Nature Communications, v. 11, no. 1, p. 1–8, https://doi.org /10.1038/s41467-019-14252-5.
- Read, A.S., Karlstrom, K.E., Connell, S.D., Kirby, E., Ferguson, C.A., Ilg, B., Osburn, G.R., Van Hart, D., and Pazzaglia, F.J., 1999, Geology of the Sandia Crest Quadrangle, Bernalillo and Sandoval Counties, New Mexico: New Mexico Bureau of Mines and Mineral Resources Geologic Map OF-GM-6, scale 1:24,000, https://geoinfo.nmt.edu/publications/maps/geologic/ofgm/downloads/6/OFGM-6\_SandiaCrest\_Report.pdf.
- Reiners, P.W., Chan, M.A., and Evenson, N.S., 2014, (U-Th)/He geochronology and chemical compositions of diagenetic cement, concretions, and fracture-filling oxide minerals in Mesozoic sandstones of the Colorado Plateau: Geological Society of America Bulletin, v. 126, p. 1363–1383, https:// doi.org/10.1130/B30983.1.
- Rice, J.R., 2006, Heating and weakening of faults during earthquake slip: Journal of Geophysical Research–Solid Earth, v. 111, B05311, https://doi.org/10.1029/2005JB004006.
- Rice, J.R., and Ruina, A.L., 1983, Stability of steady frictional slipping: Journal of Applied Mechanics, v. 50, p. 343–349, https://doi.org/10.1115/1.3167042.
- Ricketts, J.W., Karlstrom, K.E., Priewisch, A., Crossey, L.J., Polyak, V.J., and Asmerom, Y., 2014, Quaternary extension in the Rio Grande rift at elevated strain rates recorded in travertine deposits, central New Mexico: Lithosphere, v. 6, no. 1, p. 3–16, https://doi.org/10.1130/L278.1.
- Ricketts, J.W., Kelley, S.A., Karlstrom, K.E., Schmandt, B., Donahue, M.S., and van Wijk, J., 2015, Synchronous opening of the Rio Grande rift along its entire length at 25–10 Ma supported by apatite (U-Th)/He and fission-track thermochronology, and evaluation of possible driving mechanisms: Geological Society of America Bulletin, v. 128, no. 3–4, p. 397–424, https://doi.org/10.1130/B31223.1.
- Rosière, C.A., Siemes, H., Quade, H., Brokmeier, H.G., and Jansen, E.M., 2001, Microstructures, textures and deformation mechanisms in hematite: Journal of Structural Geology, v. 23, no. 9, p. 1429–1440, https://doi.org/10.1016/S0191-8141 (01)00009-8.
- Rosière, C.A., Garcia, O.L., Siemes, H., and Schaeben, H., 2013, Domainal fabrics of hematite in schistose, shear zone-hosted high-grade Fe ores: The product of the interplay between deformation and mineralization: Journal of

- Structural Geology, v. 55, p. 150–166, https://doi.org/10.1016/j.jsg.2013.07.017.
- Rowe, C.D., and Griffith, W.A., 2015, Do faults preserve a record of seismic slip: A second opinion: Journal of Structural Geology, v. 78. p. 1–26. https://doi.org/10.1016/j.isg.2015.06.006.
- Rowe, C.D., Lamothe, K., Rempe, M., Andrews, M., Mitchell, T.M., Di Toro, G., White, J.C., and Aretusini, S., 2019, Earthquake lubrication and healing explained by amorphous nanosilica: Nature Communications, v. 10, no. 1, p. 1–11, https://doi.org/10.1038/s41467-018-08238-v.
- Russell, L.R., and Snelson, S., 1994, Structure and tectonics of the Albuquerque Basin segment of the Rio Grande rift: Insights from reflection seismic data, *in* Keller, G.R., and Cather, S.M., eds., Basins of the Rio Grande Rift: Structure, Stratigraphy, and Tectonic Setting: Geological Society of America Special Paper 291, p. 83–112, https://doi.org/10.1130/SPE291-p83
- Sanders, R.E., Heizler, M.T., and Goodwin, L.B., 2006, <sup>40</sup>Ar/<sup>59</sup>Ar thermochronology constraints on the timing of Proterozoic basement exhumation and fault ancestry, southern Sangre de Cristo Range, New Mexico: Geological Society of America Bulletin, v. 118, no. 11–12, p. 1489–1506, https://doi.org/10.1130/B25857.1.
- Scholz, C.H., 1998, Earthquakes and friction laws: Nature, v. 391, no. 6662, p. 37–42, https://doi.org/10.1038/34097.
- Shimamoto, T., and Logan, J.M., 1981, Effects of simulated clay gouges on the sliding behavior of Tennessee sandstone: Tectonophysics, v. 75, no. 3–4, p. 243–255, https://doi.org/10.1016/0040-1951(81)90276-6.
- Siemes, H., Klingenberg, B., Rybacki, E., Naumann, M., Schäfer, W., Jansen, E., and Rosière, C.A., 2003, Texture, microstructure, and strength of hematite ores experimentally deformed in the temperature range 600–1100 °C and at strain rates between 10-4 and 10-6 s-1: Journal of Structural Geology, v. 25,

- no. 9, p. 1371–1391, https://doi.org/10.1016/S0191-8141(02) 00184-0.
- Siemes, H., Klingenberg, B., Rybacki, E., Naumann, M., Schäfer, W., Jansen, E., and Kunze, K., 2008, Glide systems of hematite single crystals in deformation experiments: Ore Geology Reviews, v. 33, no. 3–4, p. 255–279, https://doi.org/10.1016/j .oregeorev.2006.03.007.
- Siemes, H., Rybacki, E., Kunze, K., Klingenberg, B., Naumann, M., Brokmeier, H.G., and Jansen, E., 2010, Development of microstructure and texture of hematite ores deformed to large strain in torsion: Can texture identify the prevailing strength and creep mechanisms during deformation?: Advanced Engineering Materials, v. 12, no. 10, p. 1003–1007, https://doi.org/10.1002/adem.201000069.
- Siemes, H., Rybacki, E., Klingenberg, B., and Rosière, C.A., 2011, Development of a recrystallized grain size piezometer for hematite based on high-temperature torsion experiments: European Journal of Mineralogy, v. 23, no. 3, p. 293–302, https://doi.org/10.1127/0935-1221/2011/0023-2103.
- Siman-Tov, S., Aharonov, E., Sagy, A., and Emmanuel, S., 2013, Nanograins form carbonate fault mirrors: Geology, v. 41, no. 6, p. 703–706, https://doi.org/10.1130/G34087.1.
- Smith, S.A.F., Di Toro, G., Kim, S., Ree, J.H., Nielsen, S., Billi, A., and Spiess, R., 2013, Coseismic recrystallization during shallow earthquake slip: Geology, v. 41, no. 1, p. 63–66, https://doi.org/10.1130/G33588.1.
- Steiger, R.H., and Wasserburg, G.J., 1966, Systematics in the Pb<sup>208</sup>\_Th<sup>232</sup>, Pb<sup>207</sup>\_U<sup>238</sup>, and Pb<sup>206</sup>\_U<sup>238</sup> systems: Journal of Geophysical Research, v. 71, no. 24, p. 6065–6090, https://doi.org/10.1029/JZ071i024p06065.
- Stünitz, H., Keulen, N., Hirose, T., and Heilbronner, R., 2010, Grain size distribution and microstructures of experimentally sheared granitoid gouge at coseismic slip rates—Criteria

- to distinguish seismic and aseismic faults?: Journal of Structural Geology, v. 32, no. 1, p. 59–69, https://doi.org/10.1016 /i.jsq.2009.08.002.
- Timmons, J.M., Karlstrom, K.E., Dehler, C.M., Geissman, J.W., and Heizler, M.T., 2001, Proterozoic multistage (ca. 1.1 and 0.8 Ga) extension recorded in the Grand Canyon Supergroup and establishment of northwest- and north-trending tectonic grains in the southwestern United States: Geological Society of America Bulletin, v. 113, p. 163–181, https://doi.org/10.1130/0016-7606(2001)113<0163:PMCAGE>2.0 CO-2
- Vallina, B., Rodriguez-Blanco, J.D., Brown, A.P., Benning, L.G., and Blanco, J.A., 2014, Enhanced magnetic coercivity of α-Fe<sub>2</sub>O<sub>3</sub> obtained from carbonated 2-line ferrihydrite: Journal of Nanoparticle Research, v. 16, no. 3, p. 1–13, https://doi.org/10.1007/s11051-014-2322-5.
- Vasconcelos, P.M., Heim, J.A., Farley, K.A., Monteiro, H., and Waltenberg, K., 2013, 40Ar/39Ar and (U-Th)/He-4He/3He geochronology of landscape evolution and channel iron deposit genesis at Lynn Peak, Western Australia: Geochimica et Cosmochimica Acta, v. 117, p. 283–312, https://doi.org/10.1016/j.gca.2013.03.037.
- Verberne, B.A., de Bresser, J.H., Niemeijer, A.R., Spiers, C.J., de Winter, D.M., and Plümper, O., 2013, Nanocrystalline slip zones in calcite fault gouge show intense crystallographic preferred orientation: Crystal plasticity at sub-seismic slip rates at 18–150 °C: Geology, v. 41, no. 8, p. 863–866, https:// doi.org/10.1130/G34279.1
- Wu, L.Y., Stuart, F.M., Di Nicola, L., Heizler, M., Benvenuti, M., and Hu, R.Z., 2019, Multi-aliquot method for determining (U+Th)/He ages of hydrothermal hematite: Returning to Elba: Chemical Geology, v. 504, p. 151–157, https://doi.org /10.1016/j.chemgeo.2018.11.005.